Topographic Effects on Internal Waves at Barkley Canyon

by

Kurtis Anstey

A thesis submitted in partial fulfilment of the requirements for the degree of

Master of Science

in the Department of Physics and Astronomy

We acknowledge and respect the lək̓ʷəŋən peoples on whose traditional territory the university stands, and the Songhees, Esquimalt, and W̱SÁNEĆ peoples whose historical relationships with the land continue to this day.

Topographic Effects on Internal Waves at Barkley Canyon

by

Kurtis Anstey

Supervisory committee

Dr. Jody Klymak, Supervisor
Department of Physics and Astronomy

Dr. Steven Mihaly, Member
Department of Physics and Astronomy

Dr. Richard Thomson, Outside Member
Department of Earth and Ocean Sciences

Abstract

Submarine canyons incising the continental shelf and slope are hot spots for topography-internal wave interactions, with elevated dissipation and mixing contributing to regional transport and biological productivity. At two Barkley Canyon sites (the continental slope below the shelf-break, and deep within the canyon), four overlapping years of horizontal velocity time-series data are used to examine the effects of irregular topography on the internal wave field. Mean currents are topographically guided at both sites, and in the canyon there is an inter-annually consistent, periodic ($\sim$ week) up-canyon flow (-700 to -900 m) above a near-bottom down-canyon layer. There is elevation of internal wave energy near topography, up to a factor of 10, 130 m above the slope, and up to a factor of 100, 230 m above the canyon bottom. All bands display weak inter-annual variability, but significant seasonality. Sub-diurnal and diurnal flows are presumably sub-inertially trapped along topography, and the diurnal band appears to be forced locally (barotropically). Both sites have high near-inertial energy. At the slope site, near-inertial energy is attenuated with depth, while in the canyon it is amplified near the bottom. Both sites show intermittent near-inertial forcing associated with wind events, downward propagation of high-mode internal waves, and the seasonal mixed-layer depth, though fewer events are observed in the canyon. Free semidiurnal internal tides are focused and reflected near critical shelf-break and canyon floor topography, and appear to experience both local and remote (baroclinic) forcing. The high-frequency internal wave continuum has enhanced energy near bottom at both sites (up to 7$\times$ the open-ocean Garrett-Munk spectrum), and inferred dissipation rates, ϵ, increasing from a background of less than 10^{-9} W kg^{-1} and reaching 10^{-7} W kg^{-1} near topography. Dissipation is most strongly correlated with the semidiurnal (M_2) constituent at both sites, with secondary contributions from the sub-diurnal (Sub$_{K_1}$) band on the slope, and the near-inertial (NI) band in the canyon. Power laws for these dependencies are $\epsilon \sim M_2^{0.83} + \mathrm{Sub}_{K1}^{0.59}$ at the slope, and $\epsilon \sim M_2^{1.47} + \mathrm{NI}^{0.24}$ in the canyon. There is evidence in spectra of a near-buoyancy frequency build-up of energy correlated with high-frequency continuum variability, with a power law fit of $P_{Sh} \sim \epsilon^{0.34 \pm 0.08}$ that is independent of site topography. Though some general results are expected from observations at other slope and canyon sites, the greater temporal extent of these data provide a uniquely long-term evaluation of such processes.

Table of Contents

List of Figures

Dedication

For Shauna, always by my side, and the family and friends who support me in everything I do.

1 Introduction

Internal waves (IW) are slow-moving, low-frequency, sub-surface gravity waves that exist within density gradients in the ocean interior (Garrett & Munk, 1979). They have horizontal wavelengths up to kilometres long, and oscillate in a range between the local Coriolis (inertial, f) and Brunt–Väisälä (buoyancy, N) frequencies (Garrett & Munk, 1979). They are forced by weather - as near-inertial (NI) IW generated by surface winds exciting currents in the mixed layer (ML) that pump energy into the interior (Garratt, 1977) - or by tides and currents moving across irregular seafloor topography, generating baroclinic internal tides (IT) and IW that can propagate through the stratified ocean (Hendershott & Garrett, 2018). As travelling IW approach irregular topography, such as continental slopes or submarine canyons, they can focus and break, leading to elevated mixing. Mixing can be linked to ocean circulation, biogeochemical cycles, weather, and long-term climate (Kunze, 2017), so it is important to understand forcing by the IW field. As incident IW and IT have varying origins, amplitudes, and frequencies, each responds differently to the influence of impacted topography. Sub-inertial IW and IT may be trapped along topography, while those that are NI or super-inertial are free to reflect and propagate through open water. By characterising the IW and IT that comprise the local IW field, it may be possible to better quantify and understand IW driven turbulence and mixing.

As the wind, currents, and tides are ever-present, IW are prevalent ocean phenomena. As early as the mid-19th century, notable scientists such as Stokes and Rayleigh were investigating properties of fluid density and stratification, essential for IW propagation (Garrett & Munk, 1979). IW were mistaken as consistent noise in early 20th-century hydrocast readings, and Ekman discussed their effects in his seminal theories on fluid mechanics (Garrett & Munk, 1979). In the late-20th century, Garrett and Munk (1979) developed the canonical Garrett-Munk (GM) spectrum defining the characteristic frequency and wavenumber continuum of open-ocean IW, to better understand their role in ocean processes. Instrumentation improved, and scientists continued to uncover the contributions of IW to physical systems of all scales, from fine-scale mixing to the large-scale meridional overturning circulation (Figure 1; Garrett & Munk, 1979). Recently, studies have linked IW generation and dissipation to the global oceanic energy budget (Carter & Gregg, 2002; Kunze et al., 2002; Terker et al., 2014; Kunze, 2017), tide and wind forcing of IW to seasonal variability of regional circulation processes (Alford et al., 2012; Thomson & Krassovski, 2015), and enhanced mixing to IW interactions with irregular topography (Nash et al., 2004; Kunze et al., 2012; Gemmrich & Klymak, 2015).

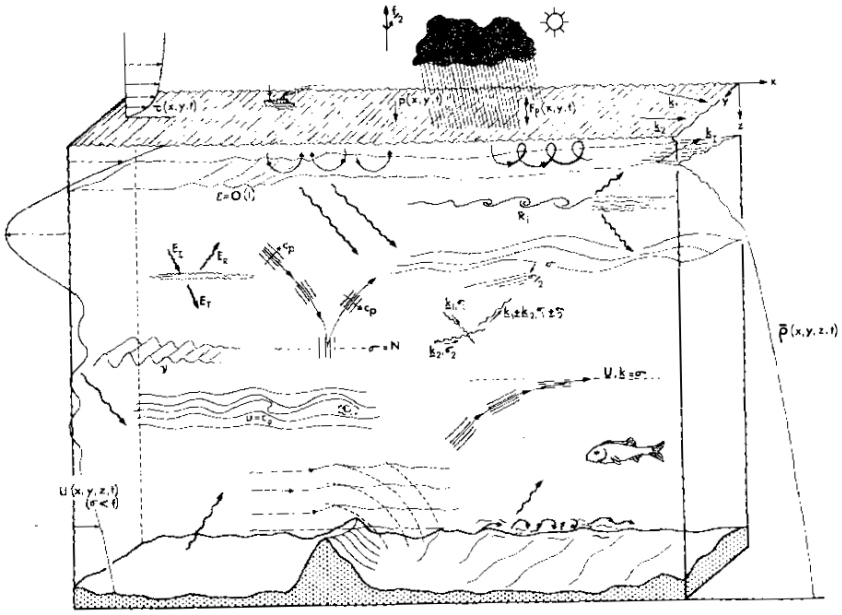

Figure 1. Generalised depiction of IW processes in the ocean, as envisioned by Garrett and Munk (1979). IW are forced by, coincide with, or contribute to most physical processes in the ocean.

Further research on IW interactions with irregular topography is thought to be essential to understanding seasonal upwelling, diapycnal mixing, and cross-shelf exchange (Burrier, 2019). As IW and IT approach seamounts, slopes, or canyons, nonlinear processes may cause their energy to reflect, scatter, or focus and break (Figure 3), dissipating as heat (Garrett & Munk, 1979; Klymak et al., 2006; Kunze et al., 2012). Dissipation leads to an energetic local environment, evident as near-bottom turbulent processes on the fine- (1 - 100 m vertical) and micro-scales ($<$ 1 m vertical) (Garrett & Munk, 1979; Carter & Gregg, 2002; Kunze et al., 2002; Kunze et al., 2012). These processes lead to the elevated mixing of pollutants and biological constituents, and drive regional transport of energy and momentum (Kunze et al., 2012). Topography-forced IW mixing helps set ocean stratification, layers that even influence the large-scale ocean-atmosphere coupled climate system (Garett & Munk, 1979).

In Canada, IW are regularly observed on the highly productive Vancouver Island Continental Shelf (VICS) (Thomson & Crawford, 1982; Allen et al., 2001), a relatively broad (about 80 km) shelf region with a canyon-incised continental slope. Regional observations have led to insight on non-linear wave-wave interactions between surface generated NI IW and upward propagating semidiurnal IT (Mihaly et al., 1998), and the presence of diurnal baroclinic shelf waves forced by tidal oscillations near the mouth of the Juan de Fuca Strait

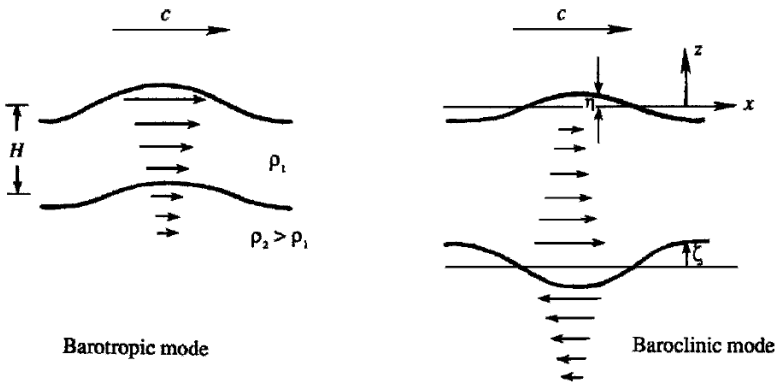

Figure 2. IW in a two-layer system. Graphic representation of the difference between barotropic and baroclinic flows. Adapted from Kundu and Cohen (2008).

(Thomson & Crawford, 1982). Seasonally variable regional currents (Thomson & Krassovski, 2015) have been associated with observations of vorticity stretching and upwelling at the head of shelf-incising Barkley Canyon, suggesting considerable influence by this canyon on VICS water properties, transport of biological constituents, and overall shelf productivity (Allen et al., 2001; Juniper et al., 2013; Doya et al., 2013; Chauvet et al., 2018). However, there is a lack of topography-IW observations at Barkley Canyon necessary to properly characterise its influence on the physical processes of the VICS. Further research into Barkley Canyon's IW field can provide insight into the effects of topography-driven mixing on the productivity of not only the VICS, but global shelf sites adjacent to canyon-incised continental slopes.

This study uses IW theory (Section 2) to evaluate horizontal velocity data from two Barkley Canyon sites (Section 3), one on the adjacent continental slope and one within the canyon, to characterise the topographic interactions of IW and IT, and their potential influence on local mixing. Mean currents (Section 4.1.1), and IW (Section 4.1.2) of sub-tidal, tidal, NI, and super-tidal (high-frequency IW continuum and near-N) frequency bands are evaluated for depth-dependence (Section 4.1.3) and seasonality (Section 4.2), including a forcing analysis of variability due to regional currents, tides, and wind. The high-frequency IW continuum (Section 4.2.5) is further evaluated for topographic influence through comparison with open-ocean GM theory, leading to approximations of dissipation and diffusivity to estimate mixing. The seasonal energy of the high-frequency continuum is correlated to low-frequency constituents to identify which bands contribute most to high-frequency turbulent processes. A near-N build-up of energy (Section 4.2.6) is also evaluated

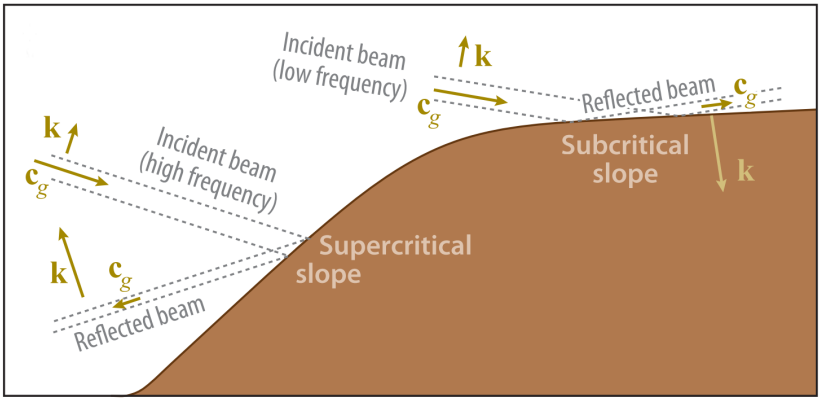

Figure 3. Graphic of IW interactions with slope topography (Lamb, 2014). The propagation angle of an IW depends on frequency and stratification. Depending on the slope of topography, incident IW can be scattered up, reflected down, or focused, possibly breaking.

for variability and energy contributions from lower frequency bands. Key findings include deep-canyon topography-guided mean current layers (Section 5.1), near-topography focusing of tidal energy with frequency-dependent seasonality and forcing (Section 5.2), attenuation of downward NI IW energy above the continental slope (Section 5.3), elevated high-frequency IW continuum energy and dissipation linked to the semidiurnal constituent (Section 5.4), and an energetic near-N band that is seasonally correlated with high-frequency continuum energy (Section 5.5).

2 Internal wave theory

Vertical displacements in a fluid can be classified as either barotropic, where the displacement is dependent only on pressure, $P(z)$ (where z is depth), or as baroclinic, where the displacement is also a function of density, $\rho(z)$, temperature, $T(z)$, etc. (Figure 2). For example, surface tides are barotropic, affecting most of the water column as the surface oscillates, while IW are baroclinic, perturbations that exist along density interfaces in the stratified ocean interior. IW are highly dependent on stratification, characterised by the depth-dependent buoyancy frequency, $N(z)$, defined as:

$$N^2(z) = -\frac{g}{\rho_0}\frac{d\rho}{dz} \tag{1}$$

where g is the acceleration due to gravity, and ρ_0 a constant reference density. In continuously stratified fluids such as the ocean interior, IW may exist both non-isotropically and rotationally, with the relative effects of clockwise (CW) and counter-clockwise (CCW) rotation described by the consistency relation:

$$\frac{CW}{CCW} = \frac{(\omega + f)^2}{(\omega - f)^2} \tag{2}$$

where ω is frequency, and f the Coriolis frequency ($f = 2\Omega\sin\phi$, where Ω is the rotation rate of the Earth, and ϕ is latitude). f and $N(z)$ are the lower and upper frequency bounds for 'free' IW (Kundu & Cohen, 2008). IW generated outside this frequency range are evanescent (trapped) to topography, unable to radiate into the ocean interior (Flather, 1988).

As free IW and IT approach irregular topography (continental slopes, submarine canyons, etc.), the angle of the incident ray to the horizontal, α, and the slope of the topography, β, have an influential relationship on the behaviour of the topography-IW interaction (Figure 3) (Lamb, 2014; Xie & Chen, 2021). The angle of incident, free IW in a continuously stratified fluid can be shown to be:

$$\alpha(z) = \sqrt{\frac{(\omega^2 - f^2)}{(N(z)^2 - \omega^2)}} \tag{3}$$

where α depends on $N(z)$, so the path tends to bend with depth (Kundu & Cohen, 2008). The impacted bathymetric slope, $\beta = \nabla H$, is determined from the gradient magnitude of the local topography, and compared with α to identify regions where IW and IT may break or reflect, known as criticality (Martini et al., 2011). For Barkley Canyon, criticality of the semidiurnal constituent is depicted in Figure 4. If $\beta > \alpha$, the slope is supercritical and incident wave

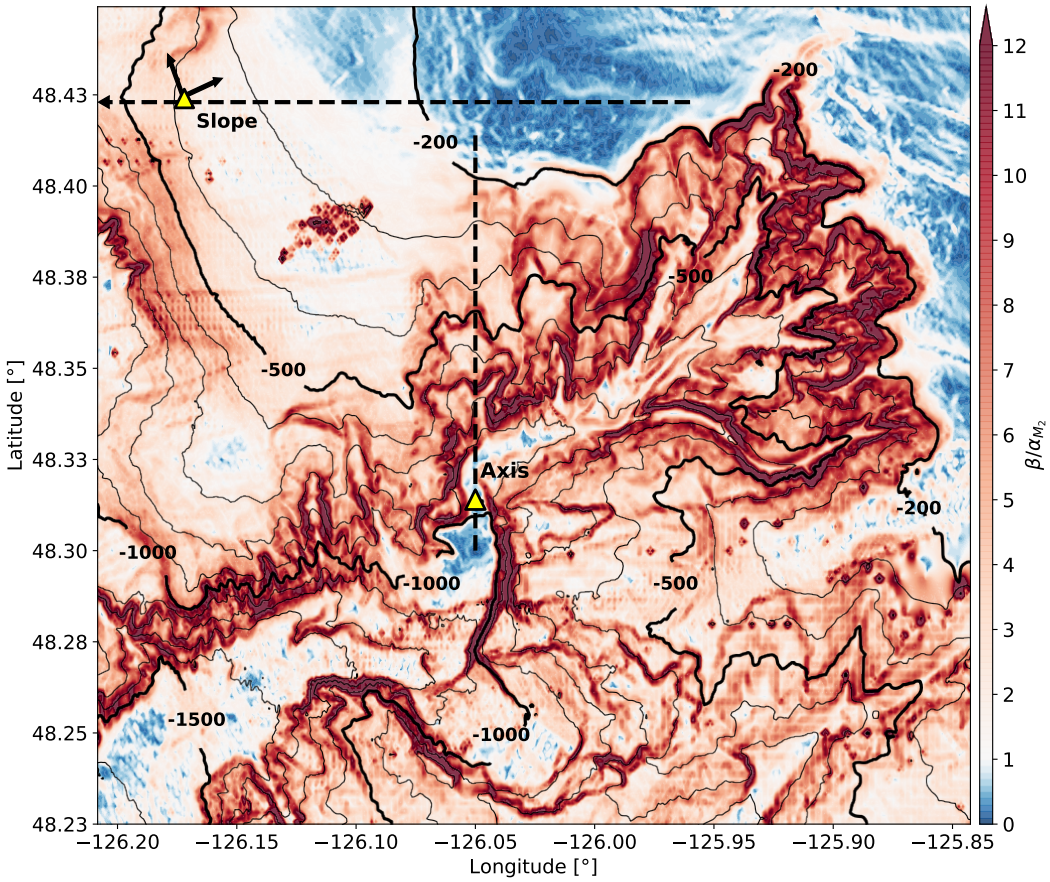

Figure 4. Site map and semidiurnal criticality of Barkley Canyon. Criticality is found by dividing the gradient slope (β) of topography by the depth-dependent semidiurnal propagation angle (α_{M2}). Most of the region is supercritical (> 1) to the M_2 IT, with notable exceptions on the shelf and canyon floor near the AXIS site. Arrows at the SLOPE site indicate 30° rotation of velocity data to match approximate along-slope (v) direction of mean currents. AXIS data were not rotated, as the along-canyon (v) component is aligned approximately N-S. Dashed black lines indicate topography cross-sections used in Figure 5. Bathymetry data obtained from NOAA (2021).

energy is reflected (see Figure 5). For $\beta \approx \alpha$, the slope is near-critical and incident wave energy is focused, potentially leading to non-linear breaking and dissipation. If $\beta < \alpha$, the slope is considered subcritical and incident wave energy is scattered (Klymak et al., 2011; Lamb, 2014). When IW reflect from near- and supercritical topography the wave frequency, angles of incidence and reflection, and energy flux are conserved (Thorpe, 2001). Meanwhile, energy density and wave amplitude increase, corresponding to decreased wavelengths and group velocity, and a focused, energetic layer near topography that is susceptible to mixing (Thorpe, 2001; Lamb, 2014). It is largely incident low mode

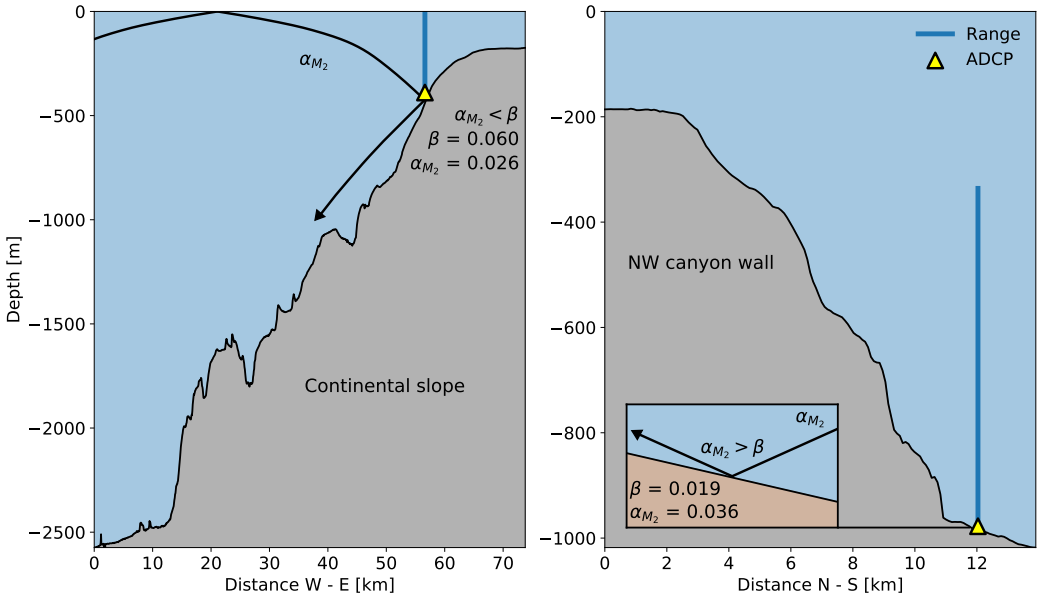

Figure 5. Site topography cross-sections with ray tracing. Depicted are the relative locations for the SLOPE (left) and AXIS (right) moorings. Horizontal cross-sections were taken in the W-E (SLOPE) and N-S (AXIS) directions, represented by the dashed black lines in Figure 4. SLOPE sits below the VICS shelf-break while AXIS is located on the floor of Barkley Canyon (right). An incident ray is shown for M_2, accounting for depth-dependent stratification, as well as local criticality at each site. α is the angle of propagation, and β the slope of the topography. In general, the SLOPE region is supercritical, while the AXIS region is both subcritical (floor) and supercritical (walls).

IW and IT, carrying energy from remote generation sites, that drive near- and supercritical reflection-based dissipation (Nash et al., 2004). It is thought that subcritical slopes only weakly dissipate low mode energy, though some models suggest that nonlinear wave-wave interactions near the bottom do contribute strongly to enhanced mixing (Xie & Chen, 2021).

Intensified near-slope layers are not uncommon (Polzin et al., 1997; Nash et al., 2004; Kunze et al., 2012), and can elevate IW energy multiple orders of magnitude with depth-dependent vertical scales hundreds of metres above bottom (Hotchkiss & Wunsch, 1982; Gemmrich & Klymak, 2015), in turn elevating mixing. These regions contribute to the generation of baroclinic IT, in addition to frictional tidal oscillations in non-critical regions (Garrett & Kunze, 2007). Topographically generated free IT can radiate away baroclinically, potentially impacting distant topography, dissipating their energy remotely (Kunze et al., 2012). Dissipation occurs when shoaling IW overturn, isopycnals steepen into unstable 'internal bores', or barotropic tidal currents generate breaking lee waves and hydraulic jumps over irregular topography (Martini et al., 2013;

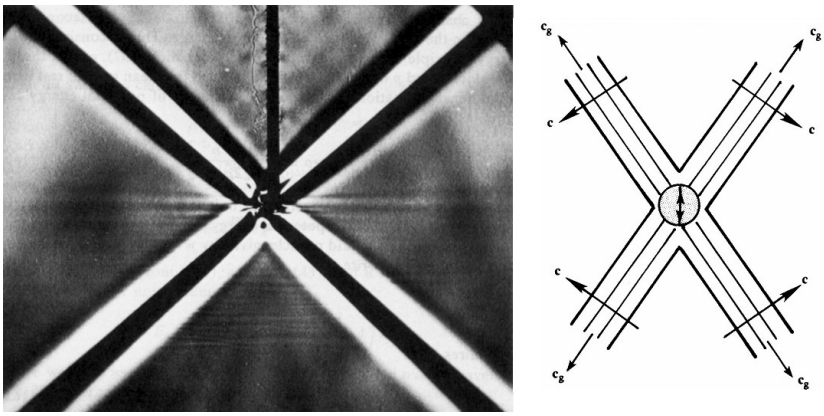

Figure 6. A photograph and graphic showing laboratory evidence for the radiation of 2D IW, from a source. Note the perpendicular phase (here indicated as c) and group velocities, and distinct propagation angles. Adapted from Kundu and Cohen (2008).

Lamb, 2014). At latitudes where generated IT are trapped to topography, baroclinic 'shelf waves' may be generated and propagate along the continental margin, where the bathymetric gradient acts as a restoring force for horizontal propagation (Crawford & Thomson, 1984; Brink, 1991).

In addition to topographically generated IW and IT, there is significant input into the oceanic IW field from wind (Alford et al., 2016). NI energy is deposited into the surface mixed-layer (ML), forcing NI currents that 'strum' IW modes. In general, the superposition of many modes forms an IW beam (Lamb, 2014), and the relative rotation and propagation of these modes moves energy downward to the base of the thermocline, then quickly into the interior (Zervakis & Levine, 1995). For a flat-bottom basin bounded by the ocean surface, the vertical structure of each IW mode strummed by the NI ML currents exists as a solution to the Sturm-Liouville equation (Alford & Zhao, 2007):

$$\frac{\partial^2}{\partial z^2}\eta(z) + \frac{N^2(z)}{c_n^2}\eta(z) = 0 \tag{4}$$

with boundary conditions $\eta(0) = \eta(D) = 0$, where D is the total water depth, η is surface displacement, n the mode number, and c_n the modal eigenspeed. Low-modes tend to dominate NI IW energy and largely propagate laterally, while high-mode energy typically radiates downward (Alford et al., 2016).

Propagation of IW and IT can be considered using a simplified 'two-wave model', first discussed in the 19th century by Rusell, Stokes, and Rayleigh, as the superposition of two waves with slightly different wavelengths that form a "slowly varying envelope" (Zhao, 2017) of energy. To describe the waves that

comprise this envelope, the horizontal dispersion relation for IW and IT is:

$$\omega^2 = f^2 + c_n^2 k^2 \tag{5}$$

where k is the horizontal wavenumber (Alford et al., 2012; Zhao, 2017). The dispersion relation can be used to find group velocity (c_g) - the velocity of the energetic envelope - and phase velocity (c_p) - the velocity of the individual waves within the envelope (Zhao, 2017), as:

$$c_g = \frac{d\omega}{dk} = \frac{c_n\sqrt{\omega^2 - f^2}}{\omega} \tag{6}$$

and

$$c_p = \frac{\omega}{k} = \frac{\omega c_n}{\sqrt{\omega^2 - f^2}} \tag{7}$$

where phase propagation is both perpendicular and vertically opposite to the motion of the envelope (Figure 6). Similarly, vertical propagation of IW energy, such as for NI IW radiating from the ML into the interior, is described by the vertical group velocity:

$$c_{gz} = \frac{\omega^2 - f^2}{\omega m} \tag{8}$$

where m is the vertical wavenumber (Alford et al., 2012; Alford et al., 2013).

3 Site and methods

Barkley Canyon

Four years of horizontal velocity data were obtained from two Barkley Canyon moorings (ONC, 2019). Located approximately 48.33°N 126.03°W, the Barkley Canyon region is 75 km southwest of the coast of Vancouver Island, incising the continental slope and VICS (Figure 4). Barkley Canyon is a winding canyon up to 6 km wide and 13 km long, with an adjacent shelf-break region at around -150 m depth. Moored acoustic Doppler current profilers (ADCP) emit acoustic beams that triangulate Doppler shifts in the water column to provide horizontal (u, v) and vertical (w) velocity time series data for Ocean Networks Canada's (ONC) NEPTUNE cabled observatory. The placement of the Barkley Canyon ADCP moorings across both continental slope and canyon topography allows for spatial comparison of coinciding IW events, while ONC's Oceans 2.0 data portal offers over a decade of processed data, allowing for typically difficult analysis of long-term variability.

Two ADCP moorings were selected for this study, located at upper continental slope (SLOPE) and canyon-floor (AXIS) sites (Figure 4). The SLOPE platform sits below the VICS shelf-break at a depth of -378 m (Figure 5), 15 km northwest of Barkley Canyon, employing primarily Teledyne RDI 75 kHz Workhorse Long Ranger ADCPs. The AXIS platform is located at a narrow north-south channel on the floor of Barkley Canyon, about midway along its length at a sharp bend, and a depth of -968 m (Figure 5), employing similar 75 kHz instruments, as well as 55 kHz Nortek Signature55 ADCPs. The Teledyne RDI 75 kHz Workhorse Long Ranger instruments were set to a vertical resolution of 8 m depth bins, and a continuous sampling rate of 2 seconds. The 55 kHz Nortek Signature55 instrument was set to a vertical resolution of 20 m depth bins, and a pulsed sampling rate of six 18-second interval pings followed by a 4.5-minute delay. For these sites, overlapping data coverage of good quality (e.g. minimal data gaps) is during 2013, 2014, 2017, and 2018 (Figure 7), due to ONC redeployment and maintenance schedules.

Processing

An initial quality check of backscatter intensity and beam correlation was performed for the raw 2-second data, yielding quality thresholds of 65 and 115 counts, respectively. For the 75 kHz RDI AXIS instruments (2013 and 2014, Figure 8) there is seasonal variation in the range of the beam-averaged intensity and correlation, notably in the fall. This is likely associated with seasonality of biological scatterers higher in the water column. The relatively shallow 75 kHz RDI SLOPE instrument, and long range of the 55 kHz Nortek AXIS instruments (2017 and 2018), yielded greater range in their QC profiles (not shown), so

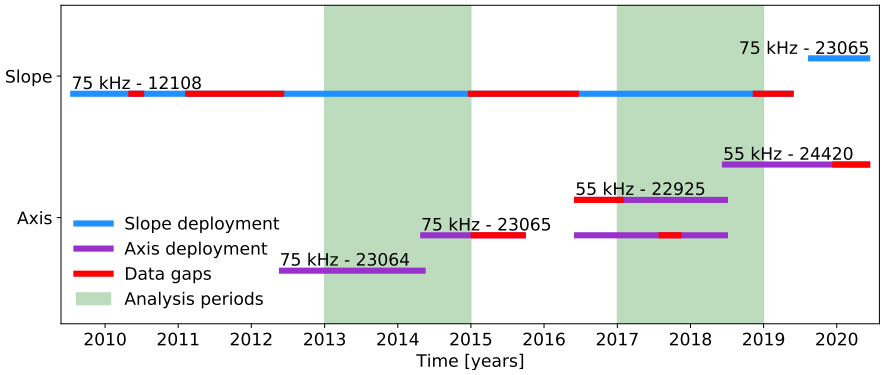

Figure 7. ADCP operating frequency, instrument ID, deployment periods, and data availability for the SLOPE and AXIS moorings. ONC operates and maintains regional instruments as part of the NEPTUNE cabled observatory (ONC, 2019). Due to maintenance and redeployments, only years with comprehensive overlapping coverage (2013, 2014, 2017, and 2018) were selected for analysis.

the 2013 and 2014 profiles at AXIS were chosen as a baseline. Time-averaged profiles indicate regions of good data ($\geq$ 90% above threshold) below -50 m at SLOPE, and below -700 m at AXIS. Masking above these depths avoids near-surface side-lobe contamination and depth-dependent processing artefacts - non-physical high-frequency spikes in power spectra obvious above about -600 m at AXIS. The expected range for the 75 kHz RDI AXIS instruments is well above -700 m, so up to -600 m is retained in plots for reference, and a dashed line at -700 m indicates the upper extent of the analysis region. For most of the analysis the 2-second high-frequency data were averaged to 15-minute blocks. All supplemental processing materials, including Python code and plots, are available in a project GitHub repository (Anstey, 2022).

At SLOPE, to better match the general cross-slope angle of approximately 30°, horizontal velocity data were rotated using a standard rotation matrix:

$$u_{rot} = u\cos(\theta) - v\sin(\theta) \tag{9}$$

$$v_{rot} = u\sin(\theta) + v\cos(\theta) \tag{10}$$

where θ is the rotation angle in radians. u is referred to as cross-slope, and v as along-slope (Figure 4). At AXIS, the along-canyon (v) alignment is already approximately north-south, and u is referred to as cross-canyon.

To account for depth-dependent stratification in spectral analysis, horizontal

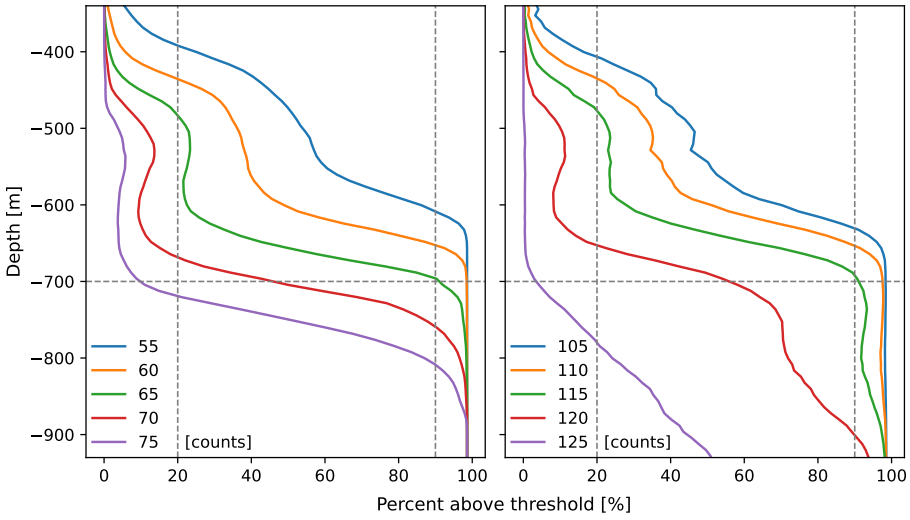

Figure 8. Axis 75 kHz backscatter intensity (left) and beam correlation (right) QC percent-above-threshold vertical profiles, for 2013 and 2014. The green line in each was selected as the ideal threshold value due to the step-function-like steepness of the profile at 20% and 90% (vertical dashed lines), in addition to the qualitative removal of depth-dependent processing artefacts above -600 m (horizontal dashed line) and near-surface side-lobe contamination, when used together as a mask.

velocity data were WKB-scaled as:

$$u_{WKB}(z) = u(z)\sqrt{\frac{N_0}{N(z)}} \tag{11}$$

and for energy density as:

$$\phi_{WKB}(z) = \phi(z)\frac{N_0}{N(z)} \tag{12}$$

with a reference buoyancy frequency of $N_0 = 2.53 \times 10^{-3}$ rad s^{-1} averaged around -900 m (Althaus et al., 2003). Buoyancy data were determined from climatology data obtained from the nearby (20 km south of Barkley Canyon) station LB14 (DFO, 2020). Data were sampled annually in May and September, during Fisheries and Oceans Canada (DFO) La Perouse cruises, casting down to -1180 m. Depth profiles were obtained for temperature, pressure, and salinity, $S(z)$, to find potential density, $\rho_\theta(z)$, following the UNESCO EOS 80 polynomial (Mamayev et al., 1991). Depth-dependent buoyancy was then determined as in Equation 1 (Figure 9). There is little inter-annual variability in the buoyancy depth profiles.

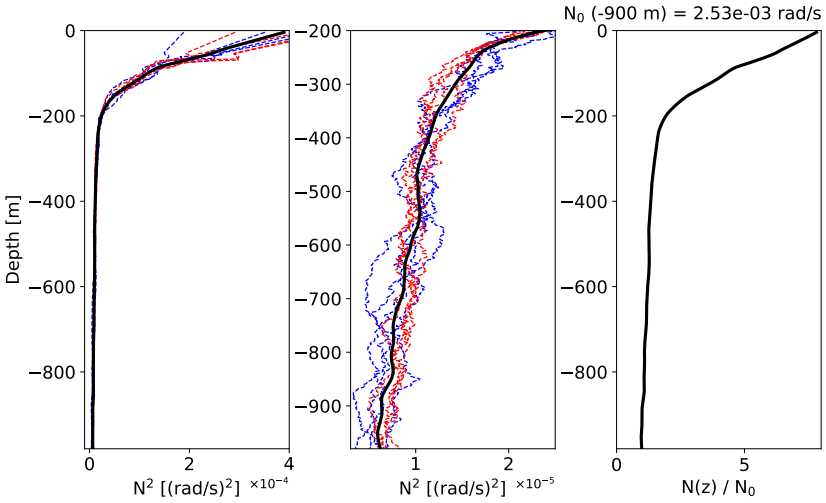

Figure 9. N^2 parameter and WKB scaling factor. Note the different depth scales, and minimal variability below -200 m. Buoyancy results were smoothed and averaged for the four analysis years of station LB14 CTD data (DFO, 2020), and are displayed through the water column (left) and below -200 m (centre). Casts were taken in May (blue) and September (red). A WKB scaling factor (right) was determined for use in Equation 12, based on N_0 averaged around -900 m.

Spectra

Component-wise power spectral density (PSD) was determined from the 15-minute averaged (Nyquist frequency of 5.55×10^{-4} Hz) WKB-scaled horizontal velocity data for each depth bin, using a Welch spectrogram process with a Hanning window of 256 data-points ($\sim$ 2.7 days), 50% overlap, and detrended in time to avoid a 0 Hz offset. Short 1.3 day and long 5.3 day spectra were also computed. The noise floor of each instrument was determined from the standard error of the mean relative to instrument sampling intervals and uncertainties from Nortek (2020) and Teledyne Marine (RDI, 2020). 95% confidence intervals were determined using a chi-squared method.

For rotational dependence, rotary power spectra were determined as for PSD, using a modified spectrogram process based on the work of Gonella (1972) and Thomson and Emery (2014). To summarise, the adjustment to find the counter-clockwise (CCW) and clockwise (CW) components of a complex horizontal velocity vector, $\boldsymbol{w}(t) = u(t) + iv(t)$, is the addition or subtraction of twice its quadrature spectrum, Q_{uv}, as:

$$\mathrm{CCW} = \frac{1}{2}[S_{uu} + S_{vv} + 2Q_{uv}] \tag{13}$$

$$\mathrm{CW} = \frac{1}{2}[S_{uu} + S_{vv} - 2Q_{uv}] \tag{14}$$

where S_{uu} and S_{vv} are the typical complex autospectra used for PSD (Thomson & Emery, 2014).

The open-ocean GM IW spectrum was determined for local parameters of $f = 1.09 \times 10^{-4}$ rad s^{-1}, $g = 9.81$ m s^{-2}, and N_0, along with canonical values for the surface-extrapolated buoyancy frequency ($N_{GM} = 5.24 \times 10^{-3}$ rad s^{-1}), e-folding scale of $N(z)$ (1.3×10^3 m), mode scale number $j* = 3$, and dimensionless IW energy parameter $E = 6.3 \times 10^{-5}$ (Munk & Wunsch, 1998; Callies, 2016). The directional GM spectrum was adapted to rotary form through application of the rotary consistency relation, as described in Section 2 (Levine, 2002; Polzin & Lvov, 2011).

Slab model

For wind forcing of NI IW, a slab model was conducted as in D'Asaro (1995) and Alford (2001), providing a simplified version of the ML response to NI wind forcing (Alford et al., 2016). Though simple, the model is continuously being improved to better account for non-homogeneous internal ML processes, and ML to pycnocline energy transfer (Alford & Zhao, 2007; Jarosz et al., 2007; Alford et al., 2016; Zheng et al., 2017; Voelker et al., 2020; Alford, 2020). From surface wind time series, wind stress is calculated as in Garratt (1977):

$$\tau_0 = \rho C_D V(z)^2 \tag{15}$$

where ρ is the density of air (approximated as 1), $V(z)$ is the complex wind velocity vector, and C_D is the characteristic drag coefficient determined by:

$$C_D \times 10^3 = 0.51 V^{0.46} \tag{16}$$

For appropriate slab model seasonality a ML of seasonally varying depth, H, must be considered. Assuming a null initialisation parameter u_{I1} at time t_1, wind generated slab layer currents at time t_2 are then computed as:

$$u_{I2} = u_{I1} e^{-\omega \Delta t} - \frac{T_t}{H\omega^2}(1 - e^{-\omega \Delta t}) \tag{17}$$

where a damped rotation frequency, ω, is determined as:

$$\omega = r + if \tag{18}$$

with $r = 0.15f$ is an artificial damping parameter, as defined in Alford (2001), and:

$$T_t = \frac{\Delta T}{\Delta t} \tag{19}$$

is related to the complex stress vector:

$$T = \frac{\tau_x + i\tau_y}{\rho_{ML}} \tag{20}$$

where $\rho_{ML} = 1024$ kg m$^{-}3$ is the average density of the ML. The slab currents are then band-passed for their NI component, u_{NI}.

4 Results

4.1 Observations

4.1.1 Mean currents

Regional low-frequency mean currents are inter-annually consistent, topographically guided, and seasonally site-dependent (Figure 10). To identify long-term mean currents, a 40-hour, 8th-order, digital low-pass Butterworth filter was applied to the horizontal velocity data. There is little inter-annual variability in mean currents, though each site has unique seasonality. At SLOPE, mean currents below -50 m are as expected for this portion of the California current system: generally poleward along-slope (up to > 0.2 m s^{-1}) through depth, with a quick transition to upwelling-favourable equatorward flow in the late-spring (April/May), with the deep poleward currents shoaling by fall (Thomson & Krassovski, 2015). In the canyon, mean currents between -700 and -900 m are consistently positive (up-canyon/landward; Figure 10 and Figure 11 - upper) up to > 0.05 m s^{-1}, with two-week rolling depth-average velocities up to 0.02 m s^{-1}, and annual means of 0.007 - 0.010 m s^{-1}. Two-month snapshots (Figure 11 - lower) show the up-canyon flow is comprised of pulses of velocity propagating upward from the bottom with periodicity of about a week. This periodicity is consistent both seasonally and inter-annually (not shown). In contrast, there is mostly down-canyon flow < 50 m above bottom.

4.1.2 High-passed currents

High-passed ($<$ 40-hour) velocity data show variable periodicity and vertical structure. Subtracting the 40-hour low-pass currents from the total yields residual high-passed currents - flows with periodicity less than 40 hours (Figure 12). A two-week snapshot during the annually recurring April/May mean current transition reveals the presence of tidal and NI IW with non-uniform vertical structure. At the SLOPE site, high-passed currents exceed 0.1 m s^{-1} in both cross- and along-slope directions, and there is periodic upward propagation above -250 m depth (about 150 m above bottom). At AXIS, high-pass currents are strongest below -750 m (about 250 m above bottom), exceeding 0.2 m s^{-1} and mostly along-canyon, with increased non-uniformity in the vertical structure above.

Annual mid-depth (-195 m and -800 m) velocity power spectra at each site show strong tidal and NI influence (Figure 13), with site- and frequency-dependent topographic guidance. Inter-annual variability is minimal (each line of the same colour is a different year), with annual spectra overlapping within a 95% confidence interval. The low-frequency sub-diurnal broadband ranges up to 1.00×10^{-5} Hz. The most defined spectral peaks are of the diurnal ($1.16 \times$

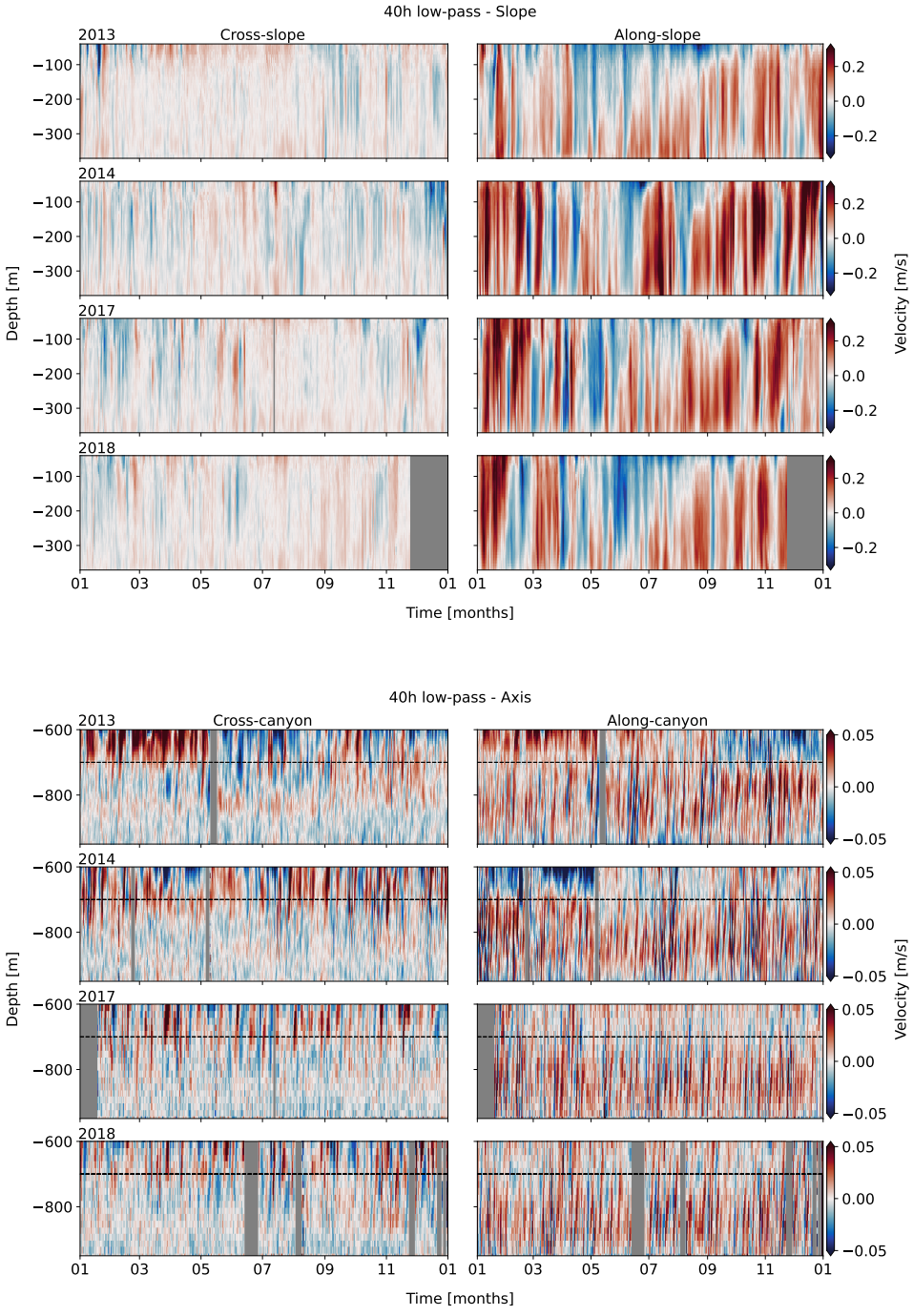

Figure 10. 40-hour low-pass horizontal velocity data for SLOPE (top) and AXIS (bottom). Components are separated as cross- (left) and along-slope/canyon (right). At AXIS, the dashed line is the upper limit of the analysis depths (-700 m). There is a clear seasonal cycle in the along-slope component at SLOPE, while seasonality is less apparent in the dominantly along-canyon flow at AXIS.

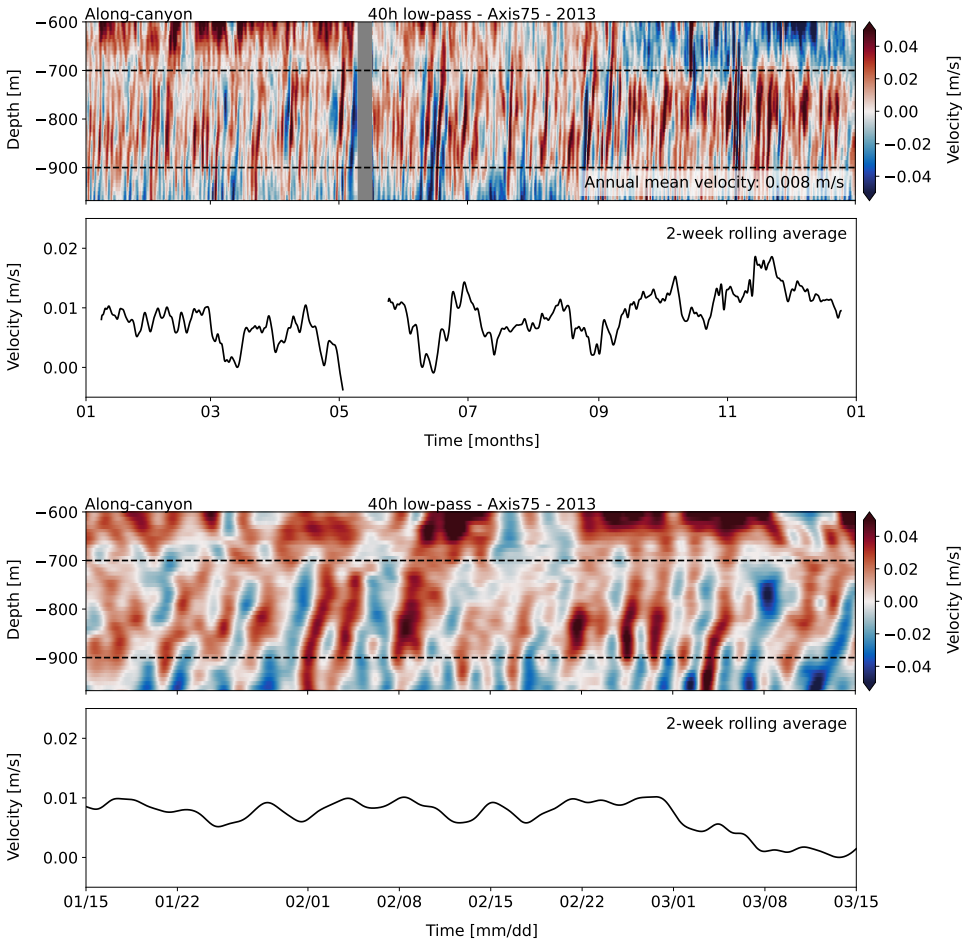

Figure 11. 40-hour low-pass horizontal velocity data showing along-canyon mean currents for AXIS, in 2013 (top) and in a two-month snapshot (bottom). Mean up-canyon flow is within the dashed lines. A thin near-bottom layer of mean down-canyon flow is below.

10^{-5} Hz), NI (1.73×10^{-5} Hz), and semidiurnal (2.24×10^{-5} Hz) frequencies. Closely associated tidal constituents (such as S_2 and M_2) were identified in high frequency-resolution spectra (not shown) as having similar topographic and seasonal responses, so shorter spectral windows are used for better seasonal resolution. Tidal constituents are therefore referred to generally (e.g. diurnal). Sum frequencies of K_1M_2, fM_2, M_4, and M_6 are evident, and are not considered further. The high-frequency IW continuum band ($7.00 \times 10^{-5} - 1.20 \times 10^{-4}$ Hz) ranges between M_6 ($\sim 6.8 \times 10^{-5}$ Hz) and an apparent energy build-up occurring near N (between $2.00 \times 10^{-4} - 1.00 \times 10^{-3}$ Hz), discussed further in Section 4.2.6.

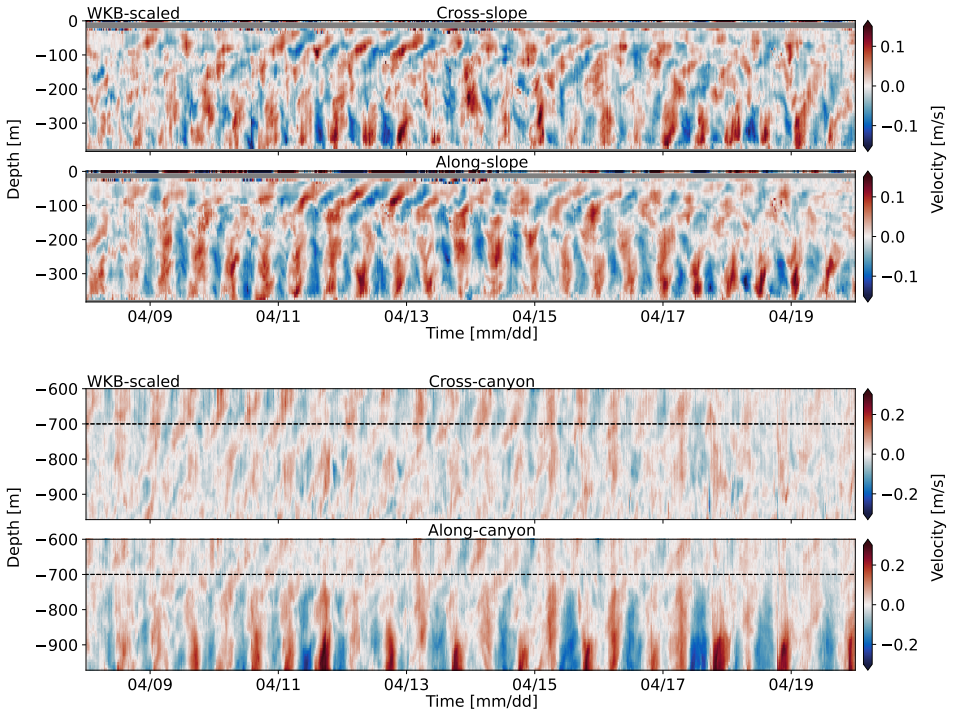

Figure 12. 40-hour high-passed WKB-scaled horizontal velocity data for SLOPE (top) and AXIS (bottom), in April 2013. Components are separated as cross- (upper) and along-slope/canyon (lower). There are IW and IT of varied frequency, non-uniform vertical structure, and depth-dependence.

At SLOPE (Figure 13 - upper), the low-frequency (sub-diurnal) flow is almost entirely along-slope (an energy ratio of up to 10:1, compared to cross-slope), with strength increasing inversely to frequency (Figure 13), indicating the importance of variability in the along-shelf currents. The diurnal constituent is strongest cross-slope (over 3:1), similar to observations by Crawford (1984; Crawford & Thomson, 1984) who noted diurnal tidal ellipses were rotated cross-slope over the Vancouver Island continental slope. The NI peak is equally distributed (1:1), indicative of rotary motion, and is indeed dominant in its CW rotary component, as expected in the northern hemisphere. The semidiurnal constituent is somewhat stronger along-slope (up to 2:1), again suggesting the influence of along-shelf currents (Rainville & Pinkel, 2006). The high-frequency continuum is slightly stronger cross-slope, and trails off slightly whiter than the expected open-ocean GM slope of -2 (discussed in Section 4.2.5). The apparent near-N build-up is partially resolved as a whitening effect, and is better observed in the raw (2-second) spectra.

At AXIS (Figure 13 - lower), compared to SLOPE, sub-diurnal power is weaker

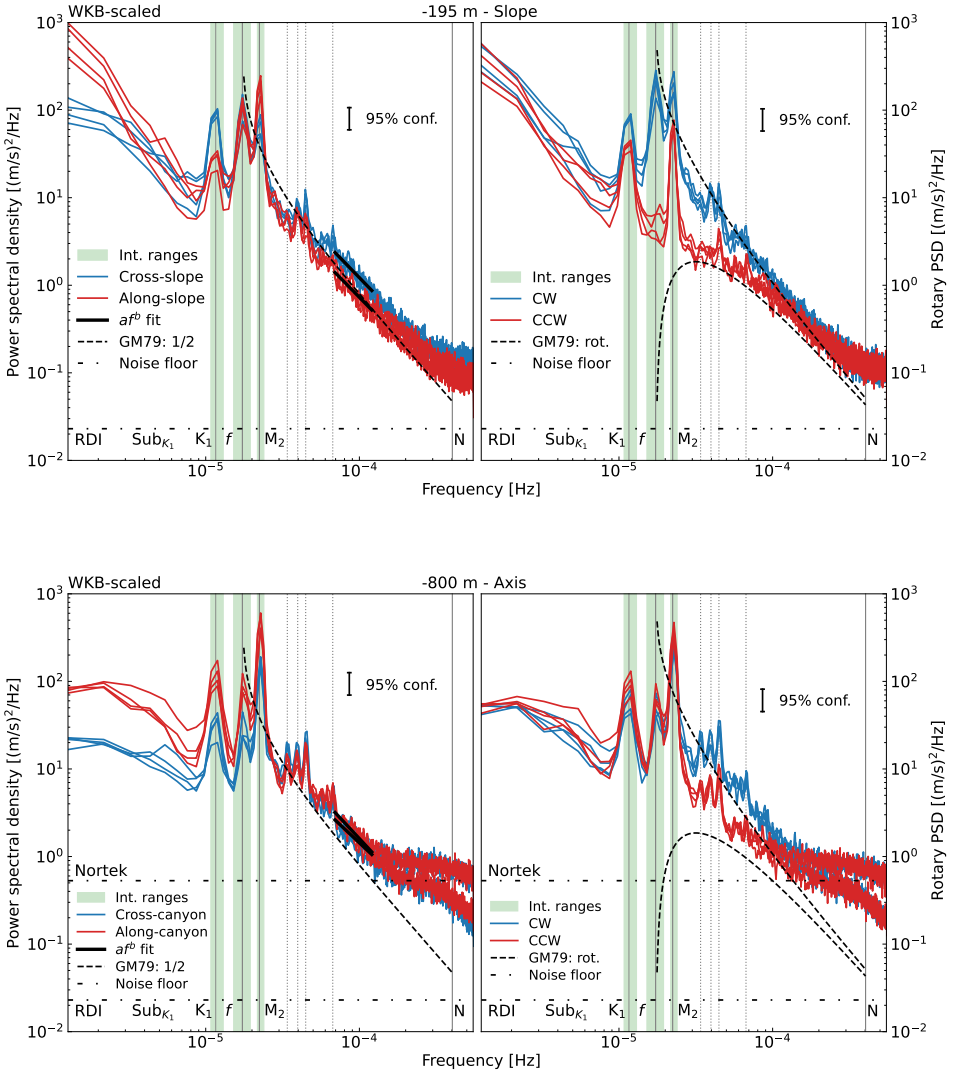

Figure 13. Mid-depth annual PSD (left) and rotary (right) spectra of WKB-scaled horizontal velocity data, for SLOPE (top) and AXIS (bottom). Each line of the same colour is a different year. For PSD, cross- (blue) and along-slope/canyon (red) components are shown. For rotary, CW (blue) and CCW (red) components are shown. 95% confidence intervals are indicated by the upper-right black bar. Dot-dashed lines show instrument noise floors. Frequency constituents with integration ranges for primary tidal and NI bands (vertical lines and green shading) are shown. Sum constituents (not discussed) are indicated by vertical dotted lines without shading, including (from left to right) K_1M_2, fM_2, M_4, and M_6. N is indicated by the vertical line to the far right. For PSD, thick black lines indicate fits to the high-frequency continuum range, and the dashed line is the GM79 spectrum (1/2 amplitude). For rotary, the GM79 spectrum is in rotary components (CW upper). Spectra at both sites are characteristically red, with tidal and NI peaks.

at frequencies below 4.00×10^{-6} Hz (Figure 13). Sub-tidal, tidal, and NI bands all trend towards along-canyon (from 3:1 at sub-diurnal, to 2:1 at semidiurnal, compared to cross-canyon), rectilinear motions. This is surprising for the NI band as a strong CW component is expected in most observations, suggesting strong topographic guidance of tidal and NI currents. Furthermore, mid-depth NI energy at AXIS is about half that at SLOPE, suggesting attenuation with depth. Above the semidiurnal peak, the super-tidal and high-frequency continuum ranges are mostly CW (about 2:1), suggesting high-frequency flows are less guided by the relatively broad canyon. Compared to SLOPE, the near-N energy build-up is obvious in 2013 and 2014, while in 2017 and 2018 the Nortek 55 kHz noise floor masks the effect.

4.1.3 Depth dependence

At each site, there is adjustment of spectral power near topography that is frequency-dependent. The WKB-scaled PSD and rotary spectra were time-averaged for annual 2D depth-frequency analysis (Figure 14). Results show a general increase (or decrease, for NI at SLOPE) in spectral energy (over an order of magnitude) in a concentrated layer $<$ a few hundred metres above bottom.

At SLOPE (Figure 14 - upper), the sub-diurnal, tidal, and high-frequency continuum bands show near-bottom intensification of IW energy. In contrast, the NI band is attenuated approaching the sea floor, below an average depth of -250 m (130 m above bottom). Near-slope adjustment is up to a factor of 10, compared to background energy. Most bands show intensification most obviously in the along-slope component, suggesting strong topographic influence, while the NI band is most obviously attenuated in its CW rotary component.

At AXIS (Figure 14 - lower), most constituents show rectilinear, along-canyon near-bottom intensification, below an average depth of -750 m depth (230 m above bottom). Near-bottom adjustment is up to a factor of 100, compared to background energy. The sub-diurnal and diurnal intensification is entirely along-canyon, with little to no power in the cross-canyon direction. The NI band, in contrast to the CW energy attenuated near the sea floor at SLOPE, has bottom-intensified flow that is almost entirely along-canyon (discussed further in Section 4.2.3). The semidiurnal intensification is strongly along-canyon, but with a medium-strength cross-canyon signal that is sharply attenuated below -900 m. High-frequency continuum strength varies between cross- and along-canyon.

A vertical scale analysis roughly agrees with the qualitative observations of enhanced layer thickness. Gemmrich and Klymak (2015) found that mode-1

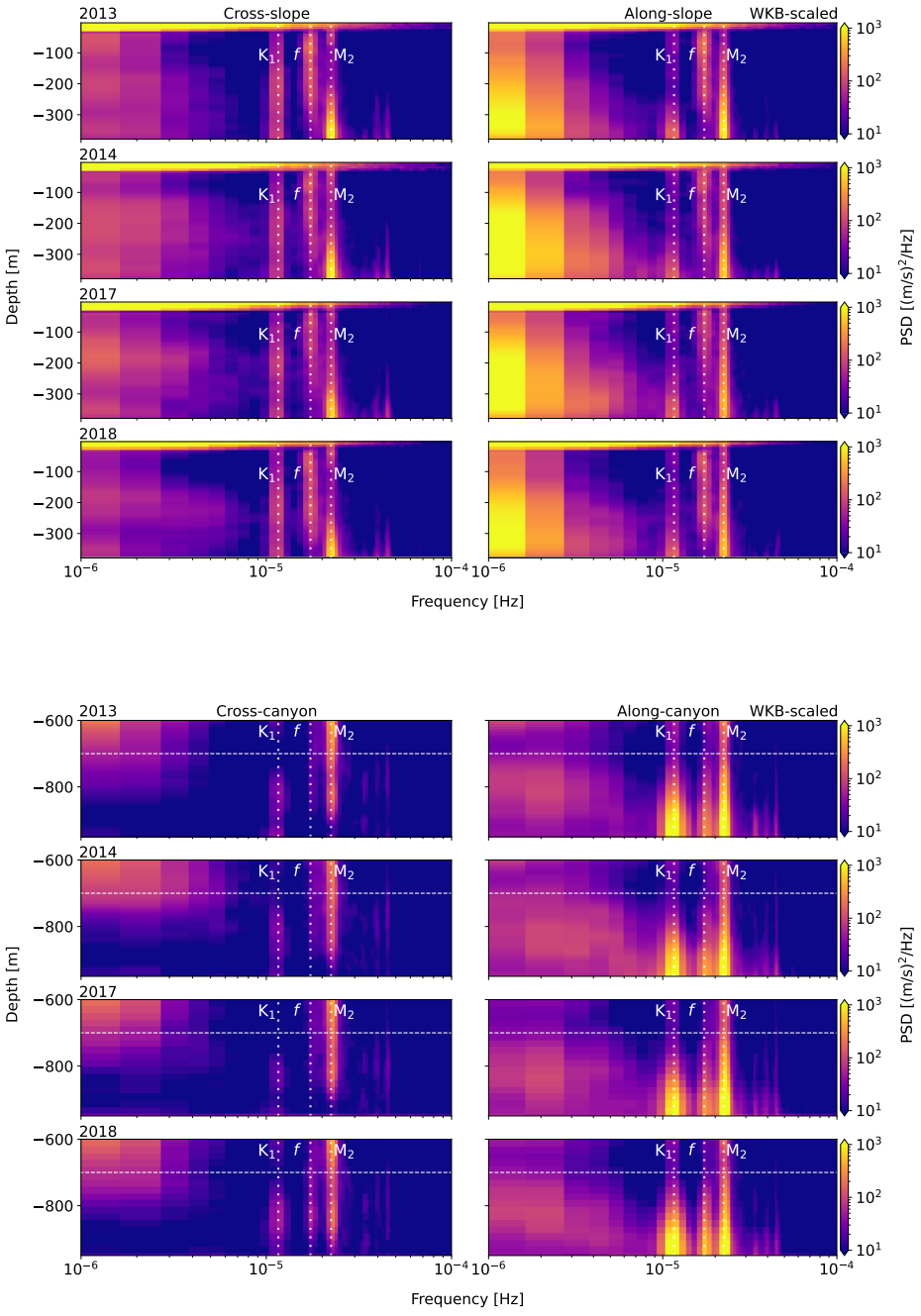

Figure 14. Depth-frequency PSD for SLOPE (top) and AXIS (bottom), determined from WKB-scaled horizontal velocity data. Components are separated as cross- (left) and along-slope/canyon (right). There is near-bottom intensification of individual frequency constituents (and near-bottom attenuation of the NI band, at SLOPE).

IW incident on sloped topography can induce a near-bottom turbulent flow layer, and that the vertical scale of the effect can be approximated as:

$$H \approx \frac{\pi U}{N} \tag{21}$$

where U is the forcing by horizontal velocity. For strong near-bottom velocities (Figure 12) and approximate buoyancy values (Figure 9) for near-topography depths at SLOPE ($U \approx 0.15$ m s^{-1} and $N \approx 3.5 \times 10^{-3}$ rad s^{-1}, at -350 m) and AXIS ($U \approx 0.25$ m s^{-1} and $N \approx 2.5 \times 10^{-3}$ rad s^{-1}, at -900 m), estimates yield vertical scales of 135 m and 314 m, respectively. Results are similar to the qualitative thickness of 130 m above bottom at SLOPE, somewhat greater than the observed 230 m above bottom at AXIS, and agree with the results of Gemmrich and Klymak (2015) for similar forcing and stratification. It should be noted that the CTD climatology data are from a nearby open-ocean site, and so do not reflect changes in stratification near topography.

4.2 Band-integrated depth and seasonal changes

There is frequency-dependent variability in the seasonality of the near-topography enhanced energy (and attenuation for NI at SLOPE). Little inter-annual variability is observed, noted only in the more intermittent sub-diurnal and NI seasonality. WKB-scaled PSD and rotary spectra were integrated over bandwidths comprising each constituent's peak or frequency range (shown as shaded green in Figure 13), for each depth bin, yielding 2D estimates of 'depth-band' power. Constituent integration ranges are sub-diurnal ($\leq 1.08 \times 10^{-5}$ Hz), diurnal ($1.08 - 1.30 \times 10^{-5}$ Hz), NI ($1.52 - 1.95 \times 10^{-5}$ Hz), semidiurnal ($2.17 - 2.39 \times 10^{-5}$ Hz), high-frequency continuum ($7.00 \times 10^{-5} - 1.20 \times 10^{-4}$ Hz), and near-N ($2.00 \times 10^{-4} - 1.00 \times 10^{-3}$ Hz).

4.2.1 Sub-diurnal

At SLOPE (Figure 15 - upper), seasonality of sub-diurnal ($\leq 1.08 \times 10^{-5}$ Hz) energy consists of intermittent pulses, strongest in fall and winter, and is one of few observations that is not inter-annually consistent. At AXIS (Figure 15 - lower), seasonality is weak, showing an occasional fall or winter pulse. A seasonal forcing analysis of the sub-diurnal constituent is inconclusive, as there is no correlation with wind or tides (not shown), or the expected low-frequency along-slope mean currents (Figure 10). Low-frequency flows can be affected by a variety of physical processes near slope, shelf, and canyon topography, such as upwelling and shelf waves (Cummins, 2000; Thomson & Emery, 2014; Thomson & Krassovski, 2015), and is likely a complex combination of regional physical processes. Further forcing analysis for the sub-diurnal range is beyond the scope of this study.

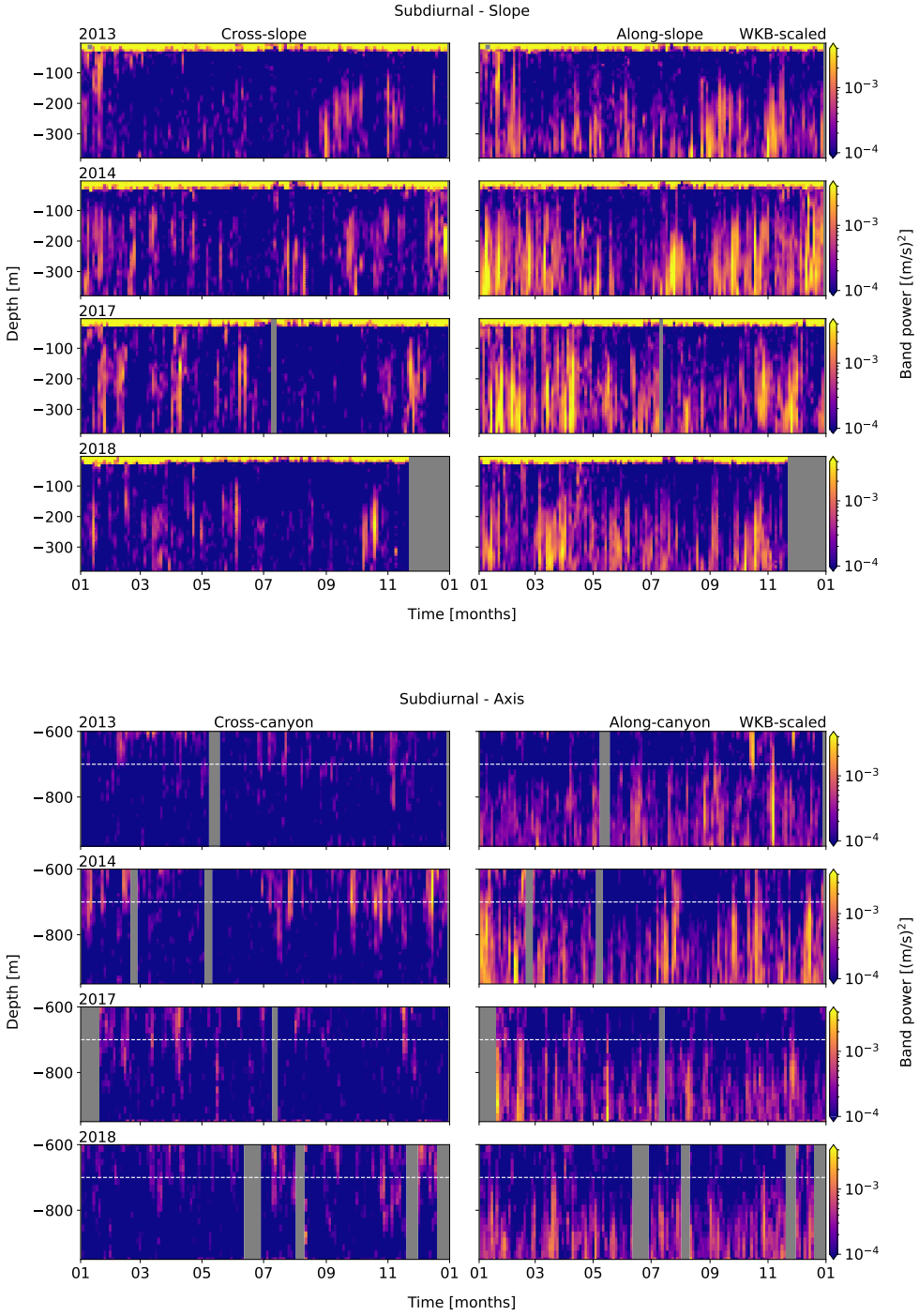

Figure 15. Band-integrated sub-diurnal PSD for SLOPE (upper) and AXIS (lower), from WKB-scaled horizontal velocity data. Cross- (left) and along-slope/canyon (right) components are shown. Each row represents an analysis year, labelled at upper-left.

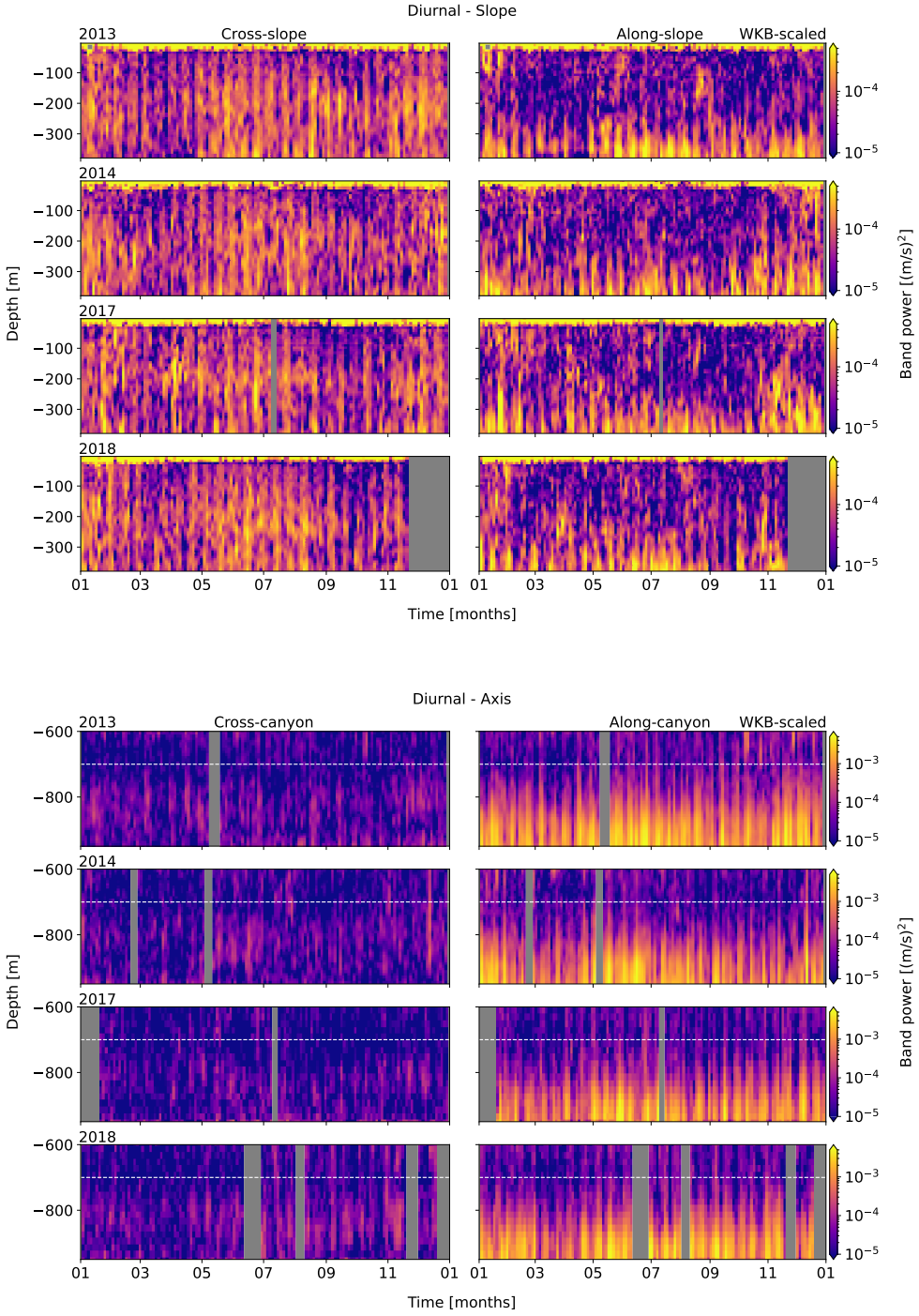

Figure 16. Band-integrated diurnal PSD for SLOPE (upper) and AXIS (lower), from WKB-scaled horizontal velocity data. Cross- (left) and along-slope/canyon (right) components are shown. Each row represents an analysis year, labelled at upper-left.

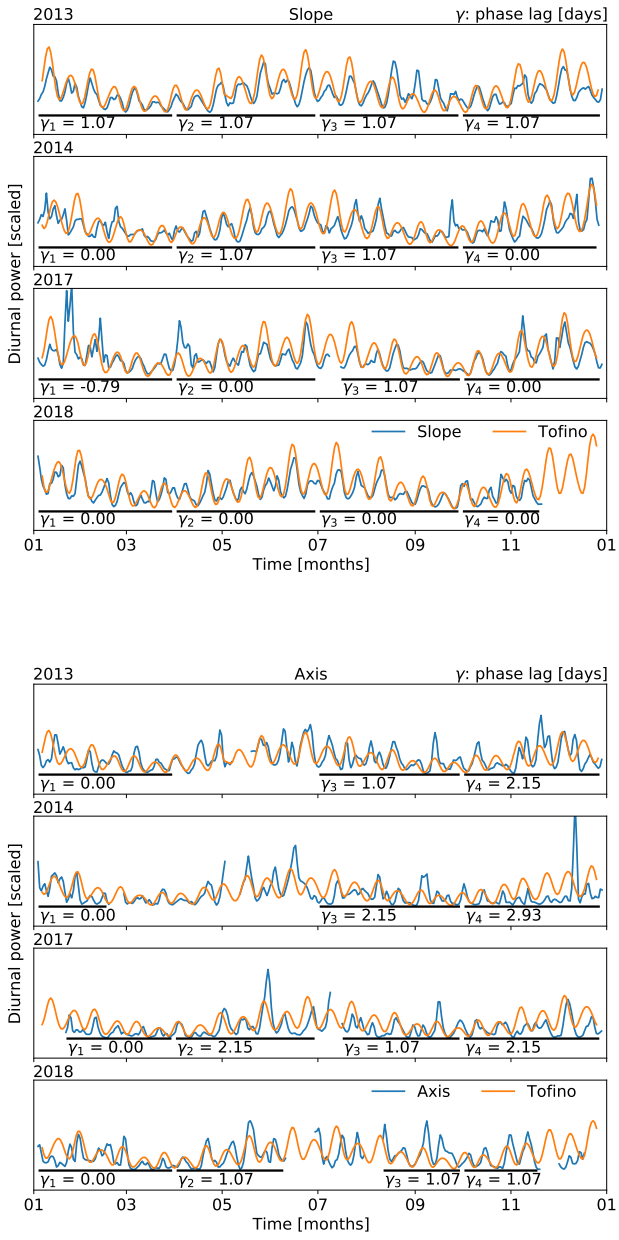

Figure 17. Diurnal barotropic forcing comparison. Phase-lag correlation and amplitude (scaled) comparisons for band-integrated power of diurnal surface level data (Tofino, orange) and WKB-scaled depth-mean diurnal power (blue) at SLOPE (top) and AXIS (bottom). Black bars indicate seasonal correlation ranges. There is a consistent yet minor phase-lag, less than the time-scale of each spectral estimate.

4.2.2 Diurnal

Diurnal ($1.08-1.30\times10^{-5}$ Hz) seasonality at SLOPE (Figure 16 - upper) is inter-annually consistent, with elevated energy late-spring through summer (months 5-8) and again (weaker) in the fall/early-winter (months 11-1). Seasonality at AXIS is not readily apparent (Figure 16 - lower).

The diurnal band is in sync with the local barotropic spring-neap cycle, fortnightly and seasonally, at both sites (Figure 17). Surface-level data were obtained from the Canadian Hydrographic Service (CHS, 2020) gauge in Tofino (station 8615), approximately 90 km due north of Barkley Canyon, as hourly time-series of deviation from chart datum, and power spectra diurnally band-passed using a similar process as for velocity observations. Comparing long-term seasonality, the Tofino barotropic spring-neap amplitudes peak in months 6-8 and 11-2, corresponding well with the diurnal observations at Barkley Canyon, and are consistent inter-annually. Fortnightly, 3-month phase-lag correlations were performed between the depth-mean diurnal power and surface-level time series, for months 1-3, 4-6, 7-9, and 10-12, each year. Phase-lag correlations range from 0 to 1 day at SLOPE (inter-annual average of 0.5 days), and 0 to 2 days at AXIS (inter-annual average of 1.1 days) - both less than the time-resolution of the spectral estimates ($\sim$ 2.7 days) used for correlations. It should be noted that AXIS estimates are only partial-depth and cannot fully resolve barotropic water-column motions, potentially contributing to observed phase offsets. Regardless, the diurnal observations are mostly in sync with both the fortnightly and seasonal local barotropic spring-neap cycle, indicating they are largely generated locally, within about 200 km Barkley Canyon (discussed in Section 5.2).

4.2.3 Near-inertial

At SLOPE (Figure 18 - upper), near-surface NI ($1.52 - 1.95 \times 10^{-5}$ Hz) seasonality is highly intermittent, with pulses occurring most likely in the fall and early-winter, though possible year-round. Some of the fall and winter NI events seen in the SLOPE data are also clear deep in AXIS observations (Figure 18 - lower). Seasonality is inter-annually consistent, but specific events are not.

For prominent pulses at SLOPE, there are periods of downward propagation of NI energy from the ML (above -50 m) to about -100 m, lasting up two weeks, after which the deep response increases quickly. At AXIS, the timing of observed pulses near the bottom appears to correspond to the delayed deep response at SLOPE. Figure 19 shows a sample event in September of 2014. A surface event deposits energy into the ML on September 3. Over the next 8 days, energy is transferred down to about -100 m. Upon reaching this depth,

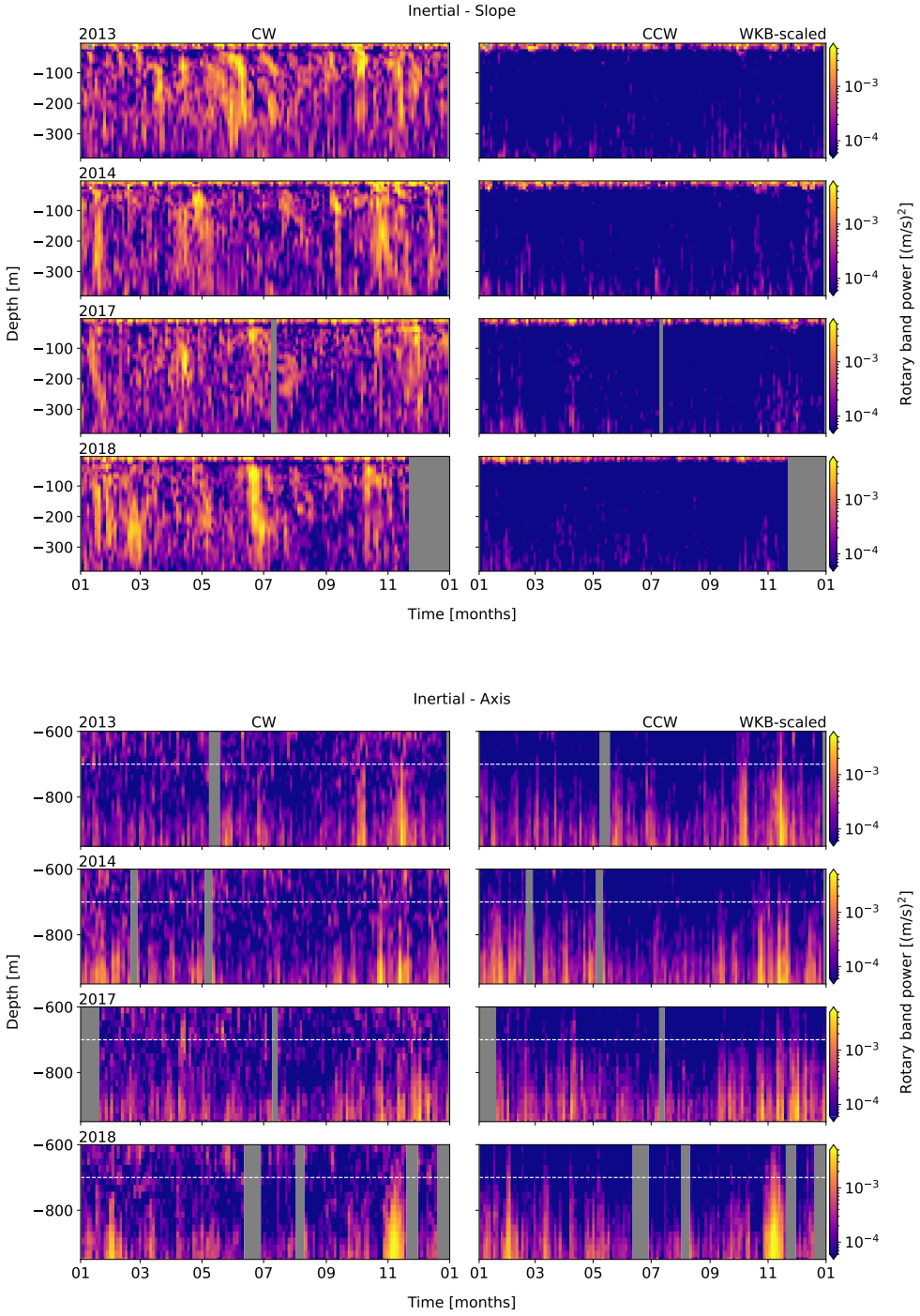

Figure 18. Band-integrated NI rotary PSD for SLOPE (upper) and AXIS (lower), from WKB-scaled horizontal velocity data. CW (left) and CCW (right) components are shown. Each row represents an analysis year, labelled at upper-left.

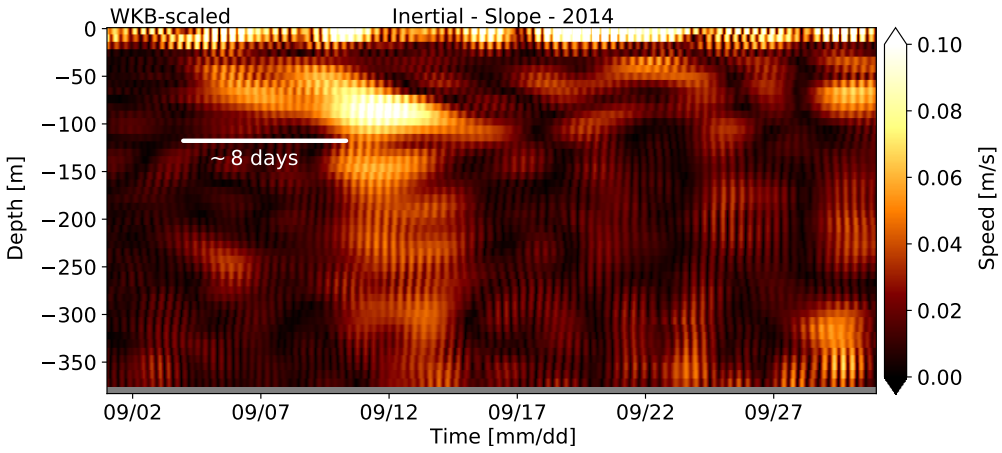

Figure 19. Transfer of NI energy in band-passed NI velocity (total) for September of 2014. A wind event (DFO, 2021) excites NI energy in the ML around September 9. Energy is transferred down to about -100 m over about 8 days, after which there is a deep response.

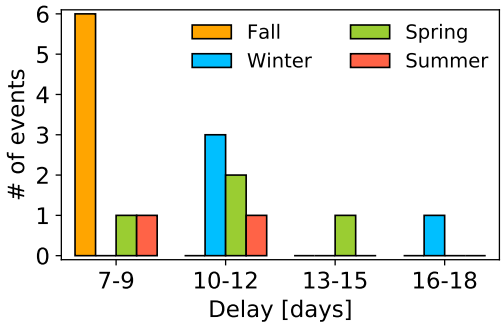

Figure 20. Histogram of delayed NI events. Delayed NI deep response events are most common and short-lived in the fall, least common in summer, and longest in the winter.

there is an immediate deep response. Energy continues to pool around -100 m, maintaining the deep response until September 14, when NI energy appears to have dissipated. There are many of these events each year, enumerated in Figure 20. The fall sees the most events, all of which are short lived, from 7-9 days, while the winter has the longest events, up to 16-18 days.

Slab model results indicate NI forcing is qualitatively linked with regional wind events, mostly in the fall and early-winter (Figure 21). Wind data were obtained from the closest Fisheries and Oceans Canada (DFO, 2021) weather buoy, La Perouse (station 46206, 50 km north of Barkley Canyon), as time series of magnitude and direction. Regional seasonally varying ML depth, H,

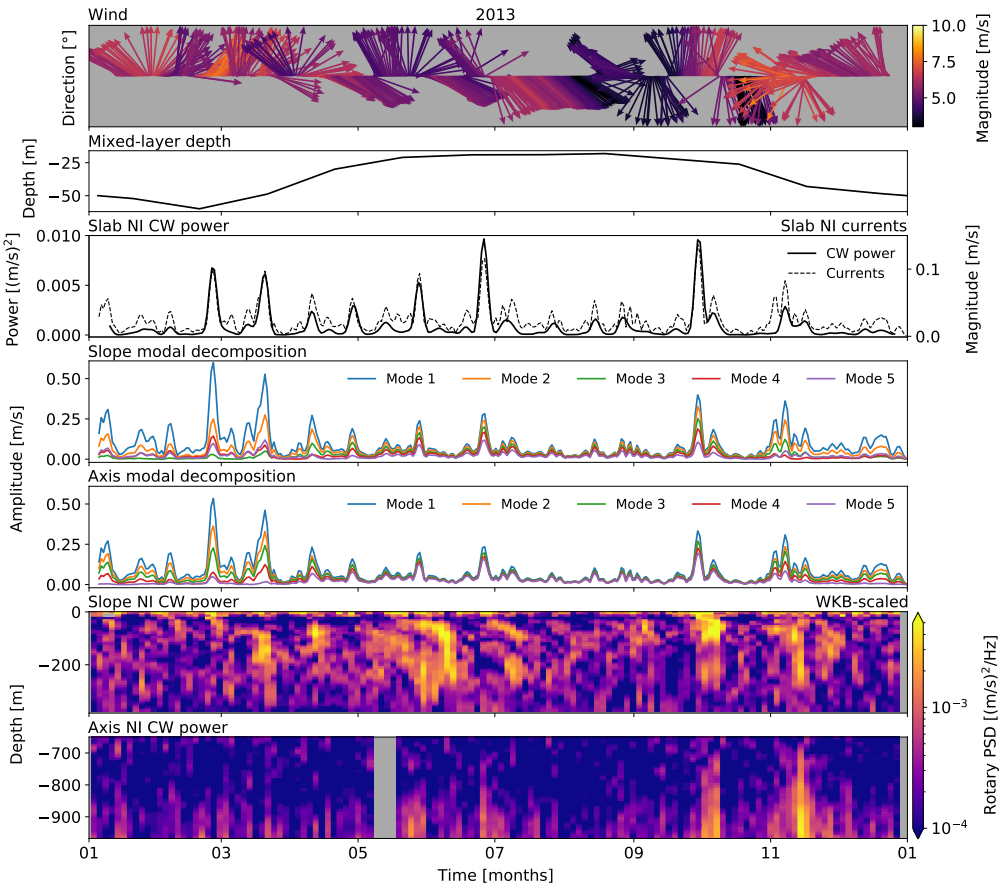

Figure 21. NI forcing analysis for 2013. From top to bottom: wind direction and amplitude (DFO, 2021); monthly-averaged ML depth for Line P station 3 as determined by Li et al. (2005); slab model NI CW power and NI currents; seasonal mode amplitudes for SLOPE and AXIS; and for reference, band-integrated NI CW power at SLOPE and AXIS. There appears to be a complex relationship between the wind, ML, slab currents, and mode amplitudes in driving the NI observations, with the most obvious effects in the fall. Due to significant data gaps, plots for other analysis years are in Appendix A.

is as defined by Thomson and Fine (2003) and Li et al. (2005) for nearby (35 km north-west of Barkley Canyon) Line P Station 3. The ML is thick in winter and spring (down to about -60 m), and thinnest summer through early-fall (up to about -20 m). There are large wind data gaps during later years (2014, 2017, and 2018), so 2013 is used as the sample year. Results for later years are available in Appendix A. Results yield time series of NI ML

currents exceeding 0.1 m s^{-1} that are qualitatively similar to wind data, most notably in the fall and early-winter. However, not every event that shows up in the ML is evident in the NI depth-band observations.

Seasonal slab model correlations (not shown) with NI depth-band power suggest interior NI response to wind forcing is strongest in summer and fall. Seasonal correlations were obtained similarly to diurnal spring-neap forcing. The slab model does poorly on a short-term basis, but if binned over three weeks the amount of energy input by the wind and found in the ADCP data shows reasonable agreement. It is possible that the apparent delay in the deep response may affect correlation with the relatively quickly influenced ML. At SLOPE, correlations are strong-positive in the fall, and medium-positive in summer. At AXIS, correlations are strong-positive in summer, and medium-positive in fall. Seasonal correlations are otherwise inconsistent, and may be further complicated by the location of the wind data buoy, 50 km north of Barkley Canyon. The fall and summer correlation periods encompass notable wind events that occur while the ML is thin and there is a more notable deep response.

Seasonally variable vertical mode projections may contribute to a greater NI deep response (Figure 21 - modal decompositions). For NI IW generation by NI ML currents, the stratification-dependent vertical mode structure is determined as described in Section 2, where the ML currents from the slab model are projected onto vertical modes. When the ML is thick, modes 1 and 2 dominate ($\sim 74\%$). When the ML is thin, contributions from low modes (1 and 2) and high modes (3, 4, 5) are about equal ($\sim 52\%$ low modes). Similar to the slab correlations, greater deep responses coincide to when the ML is thin and higher modes are equal contributors, such as in the early-fall when strong storms begin to arrive. High modes contribute most in the summer when the ML is thinnest, though there are few storms this time of year. However, even weak summer wind events occasionally warrant a deep response. In contrast, there is often little or no deep response to the many strong wind events in winter and spring when the ML is thick and low modes dominate. However, it is difficult to separate this observation from coinciding ML processes that may be more influential. A deep response associated with high-mode NI IW is not entirely unwarranted, as other studies have shown a poor local response to low-mode forcing, though the reasons are poorly understood (Gill, 1984; Zervakis & Levine, 1995; Alford, 2003). It is likely that modal analysis is a poor model, here, and that the complex balance of up and down low- and high-mode energy, along with the non-local stratification profile (Section 3), make identifying forcing of the deep response difficult.

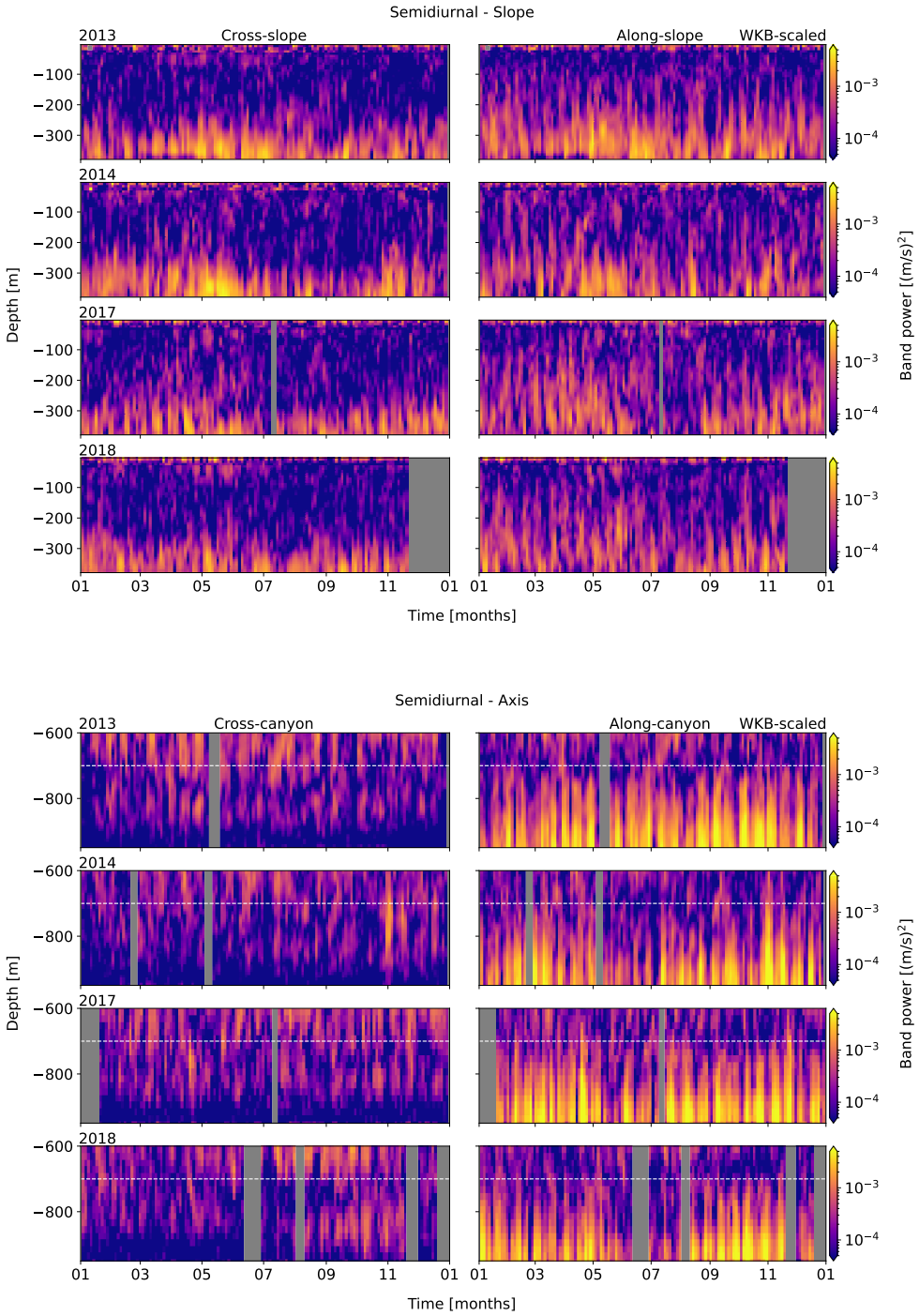

Figure 22. Band-integrated semidiurnal PSD for SLOPE (upper) and AXIS (lower), from WKB-scaled horizontal velocity data. Cross- (left) and along-slope/canyon (right) components are shown. Each row represents an analysis year, labelled at upper-left.

4.2.4 Semidiurnal

Semidiurnal ($2.17 - 2.39 \times 10^{-5}$ Hz) seasonality at SLOPE (Figure 22 - upper) is inter-annually consistent and subtle, showing a slight pulse that begins in the late-spring/early-summer (months 4/5) and an even weaker pulse in the fall/early-winter. Seasonality at AXIS (Figure 22 - lower) is not readily apparent.

Semidiurnal barotropic spring-neap forcing is intermittently in-and-out of phase, at both sites, suggesting some remote baroclinic forcing (Figure 23). Phase-lag correlations were determined as for the diurnal band. The scaled semidiurnal depth-mean band-power amplitudes vary greatly from the seasonal spring-neap surface levels. Fortnightly phase-lags are inconsistent, and for 3-month correlation periods range from 0 to 4 days at SLOPE (inter-annual average of 2.3 days), and from 0 to 6 days at AXIS (inter-annual average of 2.8 days). The irregularity of the phase-offset suggests a mix of local barotropic and remote baroclinic forcing.

4.2.5 High-frequency internal wave continuum

Variability of high-frequency IW continuum energy ($7.00 \times 10^{-5} - 1.20 \times 10^{-4}$ Hz) at SLOPE (Figure 24 - upper) is inter-annually consistent, heightened in spring through early-summer, and again through the fall. At AXIS (Figure 24 - lower), variability is less apparent, though there is generally greater energy in the fall.

At both sites, the observed high-frequency continuum amplitude is higher, and the spectral slope steeper, as compared to the open-ocean GM spectrum (Figure 25). For near-bottom depth-specific time series of WKB-scaled PSD (-300 m at SLOPE and -900 m at AXIS), a power law of af^b was fit to the high-frequency continuum band and smoothed in two week intervals, resulting in time series of power law amplitude (a) and slope (b). As the open-ocean GM spectrum can vary slightly depending on f and other parameters, a similar fit was applied to find $a_{GM,0.5} \approx 2.7 \times 10^{-9}$ m^2 s^{-2} Hz^{-1} (its energy halved to compare with observed u and v components) and $b_{GM,0.5} \approx -2.1$. At both sites, observed a ranges within $2 - 5 \times 10^{-9}$ m^2 s^{-2} Hz^{-1}, and b within -2.0 − -2.3, similar but generally higher amplitude and steeper slope compared to open-ocean GM values. Time series of power law amplitude and slope are strongly correlated, each a rough copy of depth-mean high-frequency continuum depth-band power variability (not shown).

Elevated near-topography high-frequency continuum energy leads to enhanced dissipation rates, ε, at both sites (Figure 26). WKB-scaled high-frequency continuum energy was 'whitened' over the continuum frequency range - its

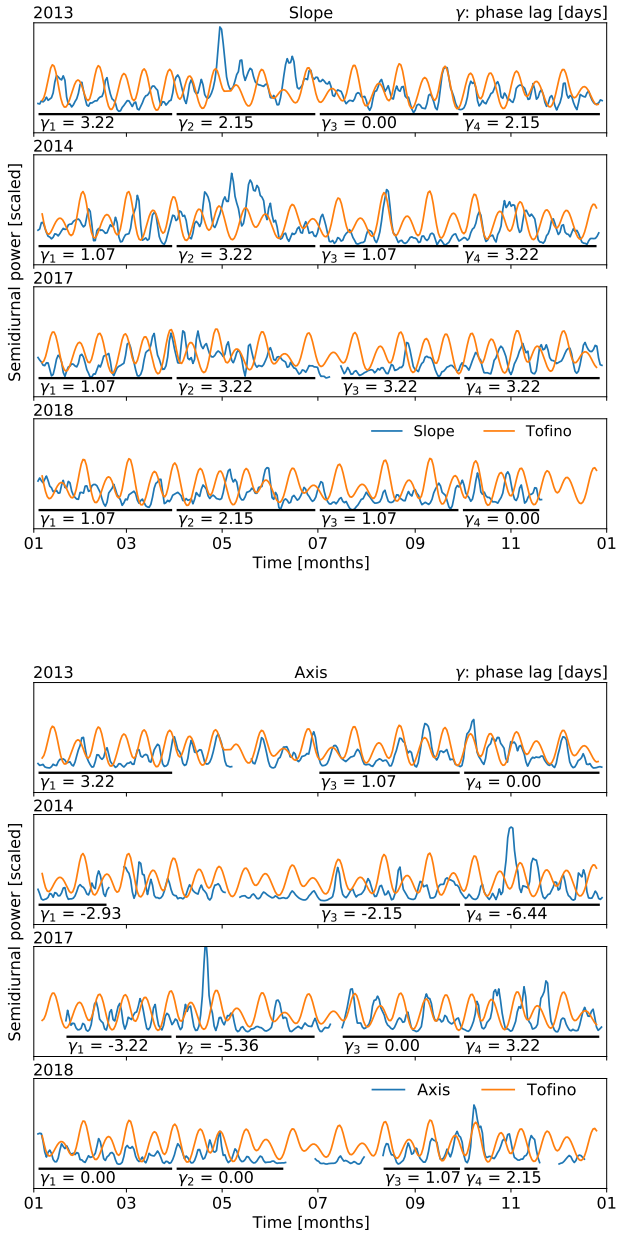

Figure 23. Semidiurnal barotropic forcing comparison. Phase and amplitude (scaled) comparisons for band-integrated power of semidiurnal surface level data (Tofino, orange) and WKB-scaled depth-mean semidiurnal power (blue) at SLOPE (top) and AXIS (bottom). Black bars indicate seasonal correlation ranges. Though the instrument amplitude is highly irregular, there is a variable phase lag that suggests a mix of local barotropic and remote baroclinic forcing.

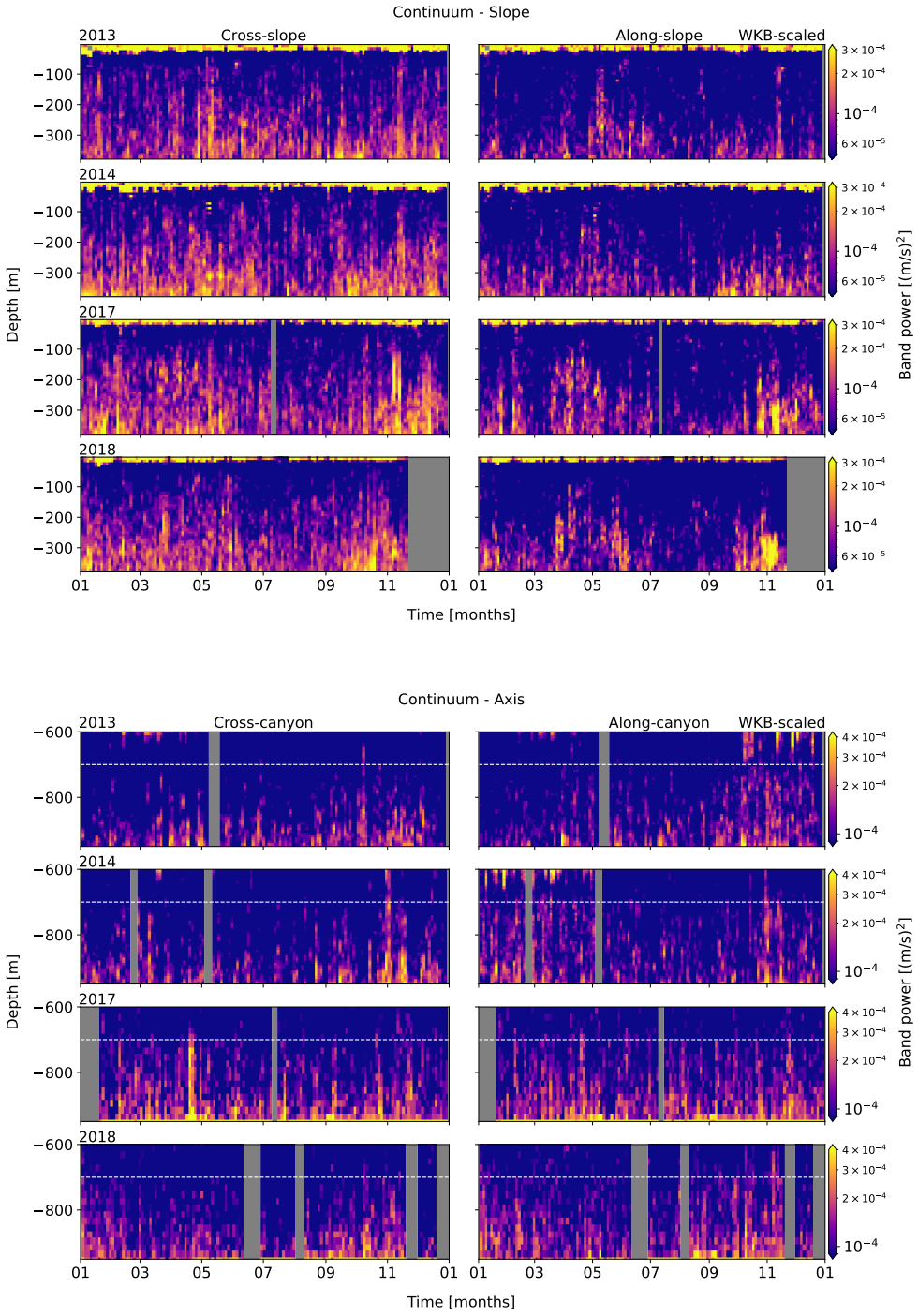

Figure 24. Band-integrated high-frequency continuum PSD for SLOPE (upper) and AXIS (lower), from WKB-scaled horizontal velocity data. Cross- (left) and along-slope/canyon (right) components are shown. Each row represents an analysis year, labelled at upper-left.

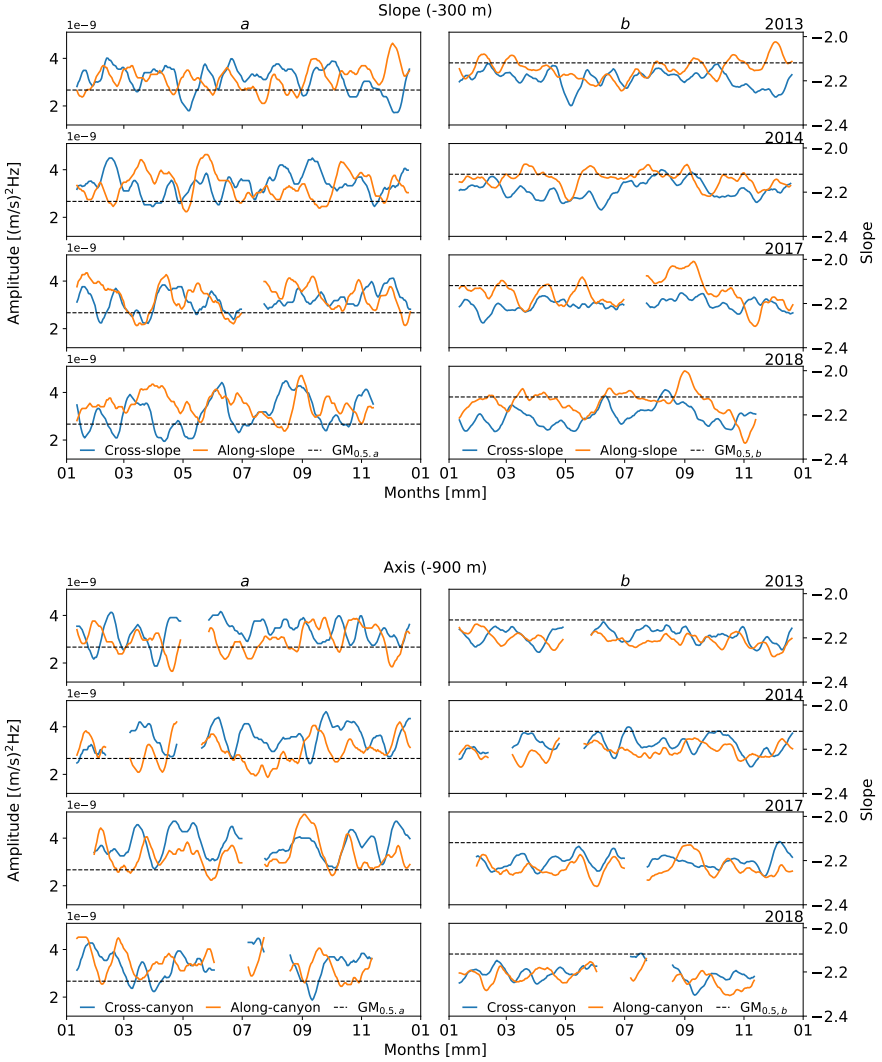

Figure 25. Time-series of high-frequency continuum power law fits. High-frequency continuum amplitude, a (left), and slope, b (right), of power law (af^b) fits to lower-depth WKB-scaled PSD, at SLOPE (top) and AXIS (bottom). For each site, each row is a year, labelled upper-right. Time series were smoothed over two weeks. Compared to GM, amplitudes are elevated up to 2× GM in the centre of a near-bottom layer of elevated energy, with spectral slopes as negative as -2.3.

power multiplied by f^2 - then averaged to find mean continuum energy, E_c, in depth and time. Determined similarly, a mean value of open-ocean GM energy was found to be $E_{GM} \approx 8.1 \times 10^{-9}$ m^2 s^{-2} Hz. The ratio of E_c/E_{GM} is up to $7\times E_{GM}$ near topography, while away from topography E_c levels fall to equal or below that of E_{GM} (not shown). From IW interaction theory (Althaus et

al., 2003), dissipation estimates were calculated from the WKB-scaled E_c fits as:

$$\varepsilon = \varepsilon_0 \frac{N_0^2}{{N_{GM}}^2} \frac{\langle {E_c}^2 \rangle^2}{\langle {E_{GM}}^2 \rangle^2} f(R_\omega) \tag{22}$$

where $\varepsilon_0 = 4.1 \times 10^{-11}$ W kg-1, $\langle {E_c}^2 \rangle^2 / \langle {E_{GM}}^2 \rangle^2$ is the measured ratio of high-frequency continuum energy to GM energy over the same frequency range, and the upper bound $f(R_\omega)$ is defined as:

$$f(R_\omega) = \left(\frac{R_\omega + 1}{R_\omega} \right)^2 \left[\cosh^{-1}(\frac{N_0}{f}) + \frac{25 \cos^{-1}(f/N_0)}{\sqrt{R_\omega}} \right] \tag{23}$$

as an energy ratio defined by Sun and Kunze (1999), with $R_\omega = 2.13$ (Kunze et al., 2002) for a high-frequency continuum with predominantly semidiurnal forcing (discussed in Section 5.4). Results reach 10^{-7} W kg^{-1} near topography, fluctuating with high-frequency continuum energy variability. Away from topography, dissipation is on the order of 10^{-9} W kg$^-1$ or less. Turbulent eddy diffusivities, κ, are similarly elevated near topography (Figure 26). From ε, diffusivity was calculated as by Osborn (1980; Kunze et al., 2002), as:

$$\kappa = \frac{\gamma \varepsilon}{N_0^2} \tag{24}$$

where $\gamma = 0.2$ is the mixing efficiency for high-Reynolds-number turbulence. Turbulent eddy diffusivities reach 10^{-3} m^2 s^{-1} near topography, again fluctuating with high-frequency continuum energy variability. Away from topography, diffusivity values are on the order of 10^{-5} m^2 s^{-1} or less, consistent with open-ocean values (Gregg, 1989; Kunze et al., 2002).

Dissipation variability (derived from high-frequency continuum energy variability) is correlated with semidiurnal forcing at both sites (Figure 27), with secondary contributions from the sub-diurnal band at SLOPE, and the NI band at AXIS. Dissipation variability correlations were determined as for NI wind forcing, for each constituent (not shown). At SLOPE, the semidiurnal band shows moderate correlations throughout the year, and strong correlations in the spring, while the sub-diurnal band shows weak to moderate correlations in both winter and spring. At AXIS, the semidiurnal band is strongly correlated all year, while the NI band is moderate to strongly correlated in the spring and fall. There is no apparent fortnightly modulation of high-frequency continuum energy or vertical scales associated with diurnal or semidiurnal spring-neap effects. To further quantify these relationships, power laws of ax^b were fit to scatter plots of depth-mean dissipation-power time series for each frequency constituent. The process was bootstrapped for improved uncertainties. At

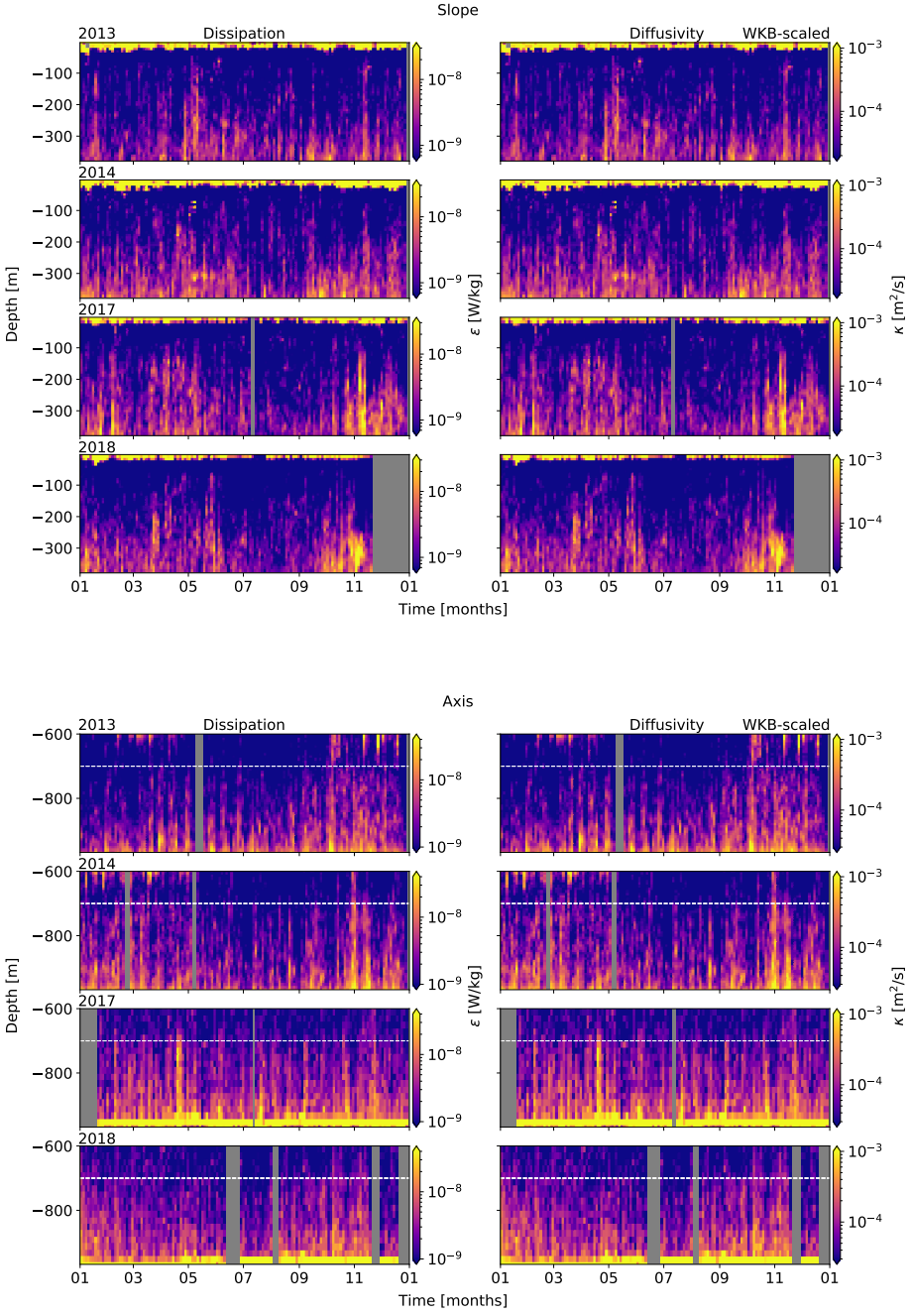

Figure 26. Dissipation rates (left) and turbulent eddy diffusivity (right), for WKB-scaled horizontal velocity spectra at SLOPE (top) and AXIS (bottom). Both dissipation and diffusivity are heightened near topography.

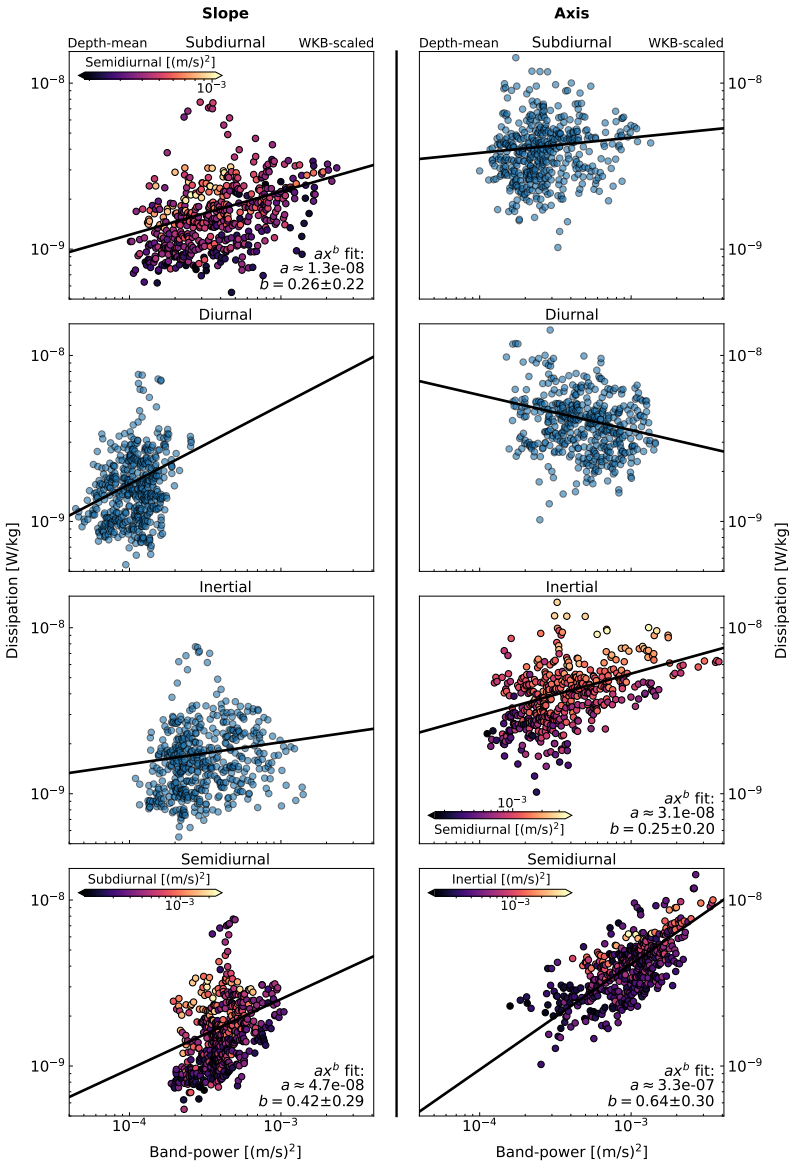

Figure 27. Dissipation power law fits. Scatter plots are for depth-mean WKB-scaled depth-band power at SLOPE (left) and AXIS (right), all years. Frequency constituents are listed for each row, as sub-diurnal (top), diurnal (second), NI (third), and semidiurnal (bottom). Black lines indicate the power law fit, listed in the lower-right of each frame. For each site, the two most likely contributors are coloured by the strength of the other.

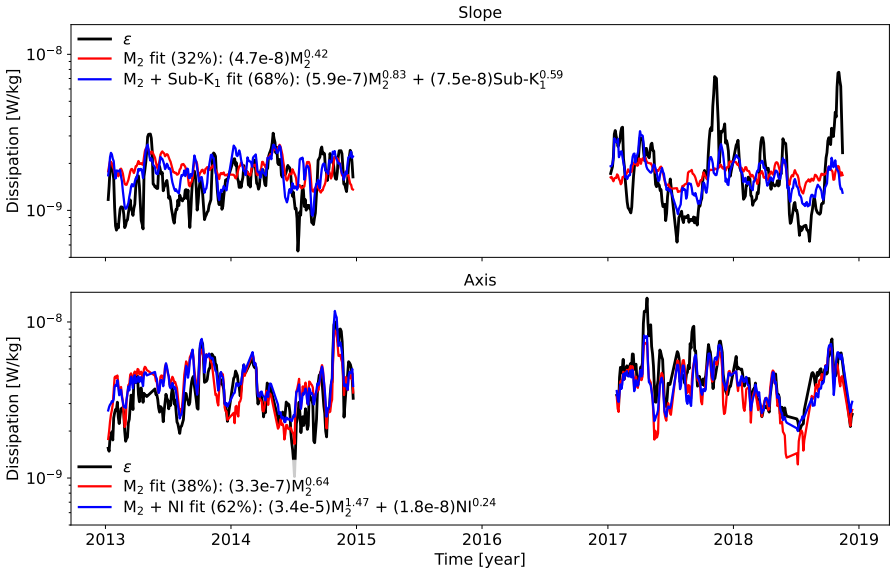

Figure 28. Dissipation multivariate power law fits for SLOPE (top) and AXIS (bottom). Shown are comparison time series of depth-mean WKB-scaled dissipation (black), semidiurnal power law fits (red), and multivariate power law fits (blue). Percent good is listed for each fit, as a measure of which fit line is closest to ε at each time step. Dissipation (black) time-series shows a seasonal trend towards a summer lull, with more energetic fall events in later years. The purely semidiurnal fits (red) are conservative in estimating periods of high and low energy at SLOPE, and often underestimate at AXIS. The multivariate fits (blue) are improved, less conservative in estimating extremes at SLOPE, and fairly accurate at AXIS.

both sites the semidiurnal band shows the best fit, and is stronger at AXIS. Secondary contributors (the sub-diurnal band at SLOPE, and the NI band at AXIS) show less obvious fits. Both the semidiurnal and secondary bands contribute to higher dissipation as they increase, but they do not drive each other. The power law fits for semidiurnal driven dissipation are $\varepsilon \sim M_2^{0.42\pm0.29}$ at SLOPE, and $\varepsilon \sim M_2^{0.64\pm0.30}$ at AXIS.

Multivariate analysis improves power law fits, reinforcing the importance of the secondary contributing constituents (Figure 28). Secondary constituents were added to the semidiurnal power law fits as $ax_1^b + cx_2^d$, where x_1 is the depth-mean semidiurnal band-power and x_2 is the secondary contributing band - sub-diurnal (Sub_{K1}) at SLOPE, and NI at AXIS. The process was again bootstrapped for improved uncertainties. Multivariate power law relationships of $\varepsilon \sim M_2^{0.83\pm0.17} + \mathrm{Sub}_{K1}^{0.59\pm0.13}$ and $\varepsilon \sim M_2^{1.47\pm0.48} + \mathrm{NI}^{0.24\pm0.06}$ were found for SLOPE and AXIS, respectively. At SLOPE, the purely semidiurnal fits are generally overestimated, and conservative in periods of high and low dissipation,

while multivariate fits are less conservative and better reflect seasonal variability. At AXIS, purely semidiurnal fits are reasonable, but generally underestimate dissipation in 2017 and 2018, while multivariate fits are fairly accurate in all years. A percent-good metric indicates the multivariate fits are better than univariate for 68% of data points at SLOPE, and 62% at AXIS.

4.2.6 Near-N

The build-up of energy at frequencies close to N (here defined between $2.00 \times 10^{-4} - 1.00 \times 10^{-3}$ Hz) is known as the near-N spectral 'shoulder' (Leder, 2002). This feature was noted by Sabinin in 1966, and only occasionally in the time since (Pinkel, 1975; Kase and Clarke, 1978; Leder, 2002; D'Asaro et al., 2007; Pinkel, 2014; Alford, 2016), as it is typically unresolved in oceanographic power spectra. The 15-minute data used in this study only partly expose this feature. To properly analyse the shoulder, 2-second data from the 75 kHz RDI instruments were obtained to allow for increased Nyquist frequency. The data for this high-frequency range were then processed similarly to the lower frequency constituents. Shoulder depth-band power is elevated near topography, though less uniformly than for lower frequency constituents (Figure 29). At SLOPE, shoulder power is mostly cross-slope and rectilinear, and somewhat intermittent in its depth-dependent enhancement. At AXIS, shoulder power is isotropic, and its depth-dependent enhancement more vertically uniform than at SLOPE. Shoulder power variability at SLOPE is subtle, somewhat heightened in the spring and fall, with intermittent brief pulses that are inconsistent in both depth and time. At AXIS, there is subtly increased energy in the fall.

However, there are multiple issues with interpreting shoulder energy variability at AXIS. During 2013 and 2014, there were adjustments to ADCP beam orientation (2013/05 and 2014/05) relative to canyon topography, an instrument swap (2014/05), and a switch from 4- to 3-beam solutions (2013/05), somehow resulting in distinct periods of higher variance (though this did not affect lower frequencies, likely due to their broader horizontal scale). These periods are defined as A)1, A_2, and A_3. A_1 is 2013/01 - 2013/09, while the first RDI 75 kHz instrument was operating with a 4-beam solution. A_2 is 2013/09 - 2014/05, after the same instrument was adjusted to a 3-beam solution, showing heightened variance up to $3\times$ A_1. A_3 is 2014/05 - 2014/12, after a new 75 kHz 3-beam instrument was swapped in, and variance was lowered to up to $2\times$ A_1. It is possible that the difference between A_2 and A_3 could be physical, as there is a coinciding drop in high-frequency continuum energy. This is possible only if high-frequency continuum energy is not (or at least not as much) affected by the instrument adjustments, which seems to be indicated in the comparative variance of raw spectra. When an orientation adjustment

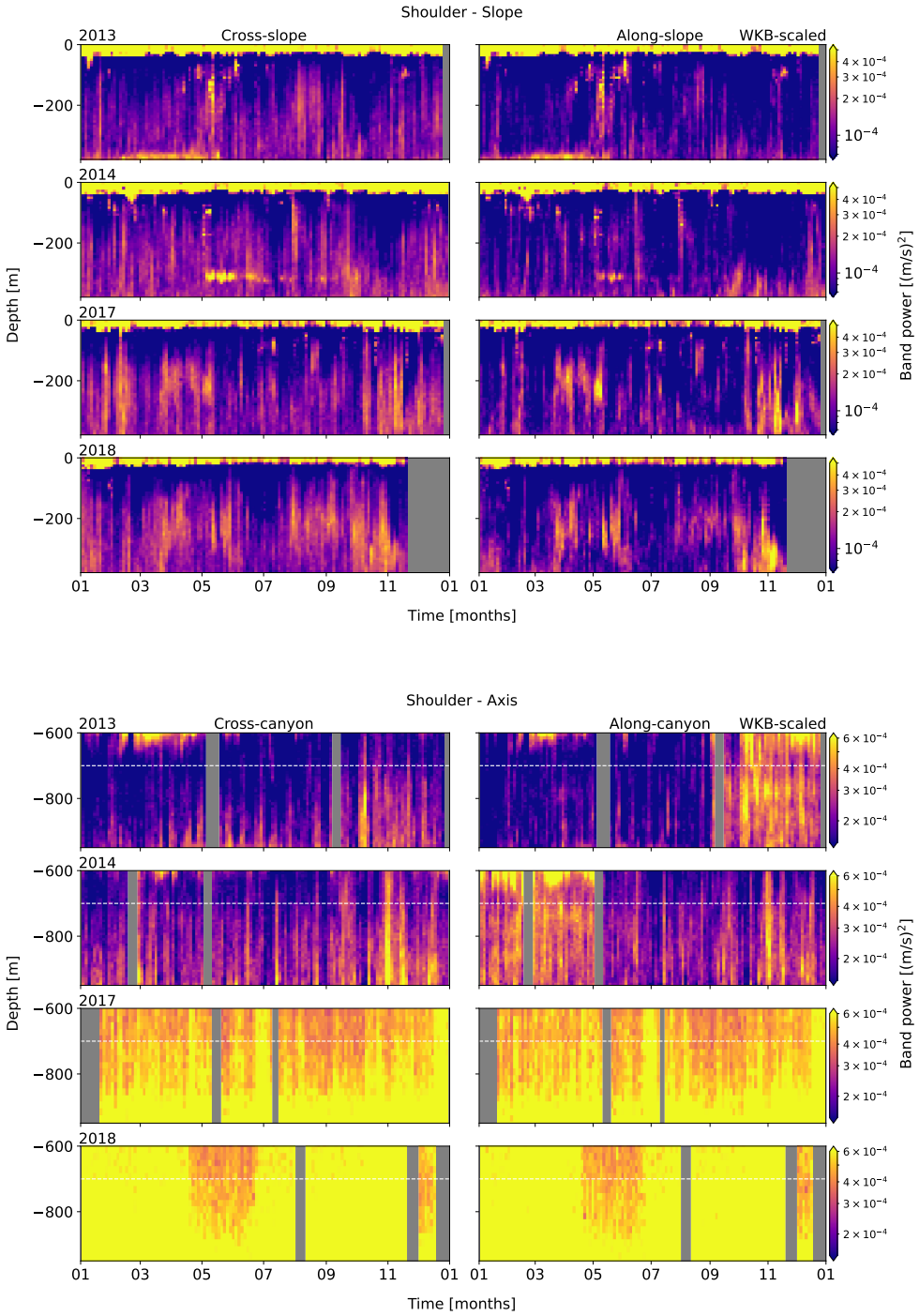

Figure 29. Band-integrated shoulder PSD for SLOPE (upper) and AXIS (lower), from WKB-scaled horizontal velocity data. Cross- (left) and along-slope/canyon (right) components are shown. Each row represents an analysis year, labelled at upper-left.

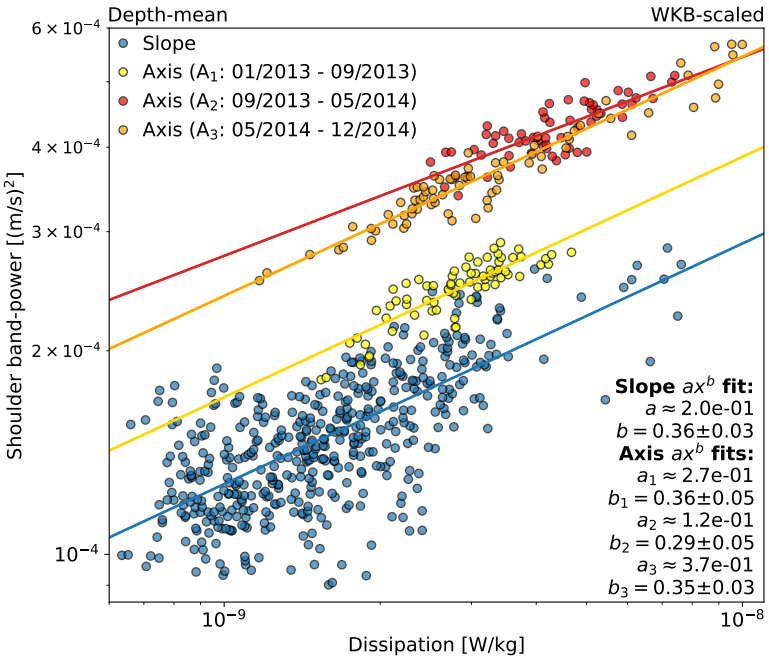

Figure 30. Power law relationship between dissipation and the spectral shoulder. Inter-annual depth-mean scatter plot for WKB-scaled dissipation and shoulder depth-band power, for SLOPE (blue) and AXIS (yellow, red, orange). SLOPE data is for all four analysis years. AXIS data is separated into three variance periods determined by instrument swaps and adjustments, for 2013 and 2014. All power law slopes agree within uncertainty, suggesting strong correlation to turbulence that does not depend on site topography.

coincided with a variance jump (as in 2014/05), the rotation was minimal (up to ∼20°), suggesting the wave field would have to be quite asymmetric to result in such a difference, which is unlikely. In 2017 and 2018, use of Nortek 55 kHz instruments at AXIS does not allow for clear resolution of the spectral shoulder, as those instruments' noise floors are higher than that of the previous Teledyne RDI 75 kHz ADCPs (Figure 13). Re-evaluation of the spectral shoulder variance at AXIS is worthwhile, but beyond the scope of this study.

There is a distinct power law relationship between turbulent dissipation (and therefore high-frequency continuum variability) and the spectral shoulder (Figure 30). Power law fits for WKB-scaled depth-mean dissipation and shoulder depth-band power (P_{Sh}) were determined as for the high-frequency continuum analysis of Section 4.2.5. At SLOPE, there is a reasonable fit of $P_{Sh\_\mathrm{SLOPE}} \sim \varepsilon^{0.36\pm0.03}$ for all four years. At AXIS, a power law was fit to each of the three variance periods in 2013 and 2014. Though amplitudes

vary between periods, power law slopes are similar, with $P_{Sh\_A_1} \sim \varepsilon^{0.36\pm0.05}$, $P_{Sh\_A_2} \sim \varepsilon^{0.29\pm0.05}$, and $P_{Sh\_A_3} \sim \varepsilon^{0.35\pm0.03}$. Power law slopes at both SLOPE and AXIS all agree within uncertainty (averaging $P_{Sh} \sim \varepsilon^{0.34\pm0.08}$), suggesting a connection between spectral shoulder energy and turbulence that does not depend on site topography. The shoulder appears to vary weakly with high-frequency continuum energy, perhaps not responding as quickly to the external forcing because of the time it takes for energy to cascade from low to high wave frequencies.

5 Discussion

5.1 Canyon axis mean currents

The periodic ($\sim$ week) up-canyon mean flow at AXIS (between -700 and -900 m), with its underlying near-bottom down-canyon layer, is notable for its seasonal and inter-annual consistency and circulation implications (close to zero net mean flow), important for understanding sediment transport and physical-biological coupling influencing VICS productivity (Xu & Noble, 2009). In previous biological studies at Barkley Canyon (Cabrera et. al, 2018; Chauvet et al., 2018), a two-layer flow system was noted similar to that of both Hudson Canyon (Hotchkiss & Wunsch, 1982) and Monterey Canyon (Xu & Noble, 2009). These systems were attributed to circulation cells caused by along-canyon pressure gradients driven by consistent large-scale quasi-geostrophic along-shelf regional currents, similar to those observed at SLOPE. The upward propagation of these currents was observed with periodicity ranging from semidiurnal at Monterey Canyon, to > than a few days at Hudson Canyon, and found to shoal at an angle similar to that of the up-slope gradient (Hotchkiss & Wunsch, 1982; Petruncio et al., 1998; Xu & Noble, 2009). Tidal rectification, where tides force an up-slope pressure gradient (Garrett, 2004), could also drive a periodic mean up-canyon flow. The associated near-bottom (< 50 m) down-canyon flow could be linked to turbidity currents, tidal resuspension, and river-flood-induced underflows, that occur as shelf sediment descends through canyons to the ocean interior (Xu & Noble, 2009; Juniper et al, 2013; Chauvet et al., 2018). At Barkley Canyon, where large-scale regional mean currents move consistently along-slope across the mouth and rim of the canyon, this seems a likely explanation. However, tidal rectification and turbidity currents cannot be ruled out.

To associate the observed AXIS mean flow with these potential forcing mechanisms, correlations were computed for the observed along-canyon periodicity and mean currents at SLOPE, fortnightly spring-neap tidal influence, and depth-mean semidiurnal depth-band power. Correlations are inconsistent (not shown), and do not suggest forcing by these sources. However, though there is no obvious connection to diurnal or semidiurnal spring-neap forcing, estimates of total lower-canyon transport (below -700 m) from depth- and time-mean annual velocities result in near-zero net up-canyon flow (annually between 0.004 - 0.005 m s^{-1}), potentially consistent with tidal rectification theory (Garrett, 2004).

Though along-canyon mean flow systems have been noted at other canyons, the periodicity and attributed forcing comparisons at Barkley Canyon do not

align with other studies, as there is little correlation to SLOPE mean currents, the spring-neap cycle, or semidiurnal energy. Speculatively, it is most likely that this circulation is driven by the strong regional mean currents that exist at SLOPE, though tidal rectification and turbidity currents may also contribute. Potential canyon resonances could also modulate periodicity (La Souëf & Allen, 2014). It is possible that such circulation may be common in shelf-incising canyons, but that forcing is dependent on unique site characteristics and regional physical processes, and so is difficult to determine. Further evaluation is necessary, and beyond the scope of this study.

5.2 Tidal currents

The diurnal and semidiurnal tidal constituents are two of the greatest sources of IW energy, and affect mean currents, mixing, IT and baroclinic shelf wave propagation, and VICS circulation and productivity (Crawford & Thomson, 1984; Cummins & Oey, 1997).

For the diurnal constituent, there is elevated energy in the late-spring and summer. Results are consistent with previous studies in the region. Drakopolous and Marsden (1993) associated strengthened diurnal tidal flow over the VICS with increased stratification in summer, while Cummins et al. (2000) suggest diurnal currents are seasonally responsive to the large-scale spring shift to equatorward, upwelling-favourable mean currents. Xu and Noble (2009) found inter-annually consistent K_1 currents in Monterey Canyon that peaked relative to the annual cycle of spring-neap tidal forcing, as observed here.

As the diurnal (and sub-diurnal) frequency is sub-inertial, diurnal IT are evanescent (trapped) to topography north of their turning latitude (~ 30°N), unable to radiate offshore. Cummins and Oey (1997) found that trapped diurnal IT generation was prevalent on the VICS adjacent continental slope, similar to other Pacific slopes (Rudnick et al., 2015) and seamounts (Robertson et al., 2017). It is unlikely for there to be incident baroclinic diurnal IW or IT unless they propagate along the shelf. However, if a diurnal spring-neap phase-lag of up to a day is present, as potentially observed at SLOPE, this suggests a remote baroclinic generation site within about 200 km, based on a K_1 mode-1 wave speed of about $c_1 \sim 2.0$ m s^{-1} (Crawford & Thomson, 1984). One candidate would be diurnal shelf waves generated by oscillatory tidal currents near the mouth of the Juan de Fuca Strait ($\sim$ 100 km east of Barkley Canyon) that propagate poleward along the VICS (Crawford & Thomson, 1984; Flather, 1988). Confirmation of such waves would require additional instruments along the shelf, and is beyond the scope of this study. Other regions thought to be productive for baroclinic diurnal waves are either

disconnected from the shelf (e.g. the abyssal Juan de Fuca Ridge) and cannot propagate sub-inertially to Barkley Canyon (Lavelie & Cannon, 2001), or too distant for the observed phase-lag (e.g. Mendocino Escarpment, 900 km south of Barkley Canyon; Morozov, 2018). As there is enough uncertainty in the correlations that the phase-lag could effectively be null, and considering the vertically linear structure present, it is likely that the diurnal band is primarily forced by the local barotropic spring-neap cycle, with possible seasonal contributions from shelf-waves, mean current interactions, or stratification.

In contrast, the semidiurnal constituent is locally super-inertial, able to freely propagate away from topography as IT. There could be incident remote semidiurnal IT at Barkley Canyon, contributing to the highly variable response. For a semidiurnal phase-lag up to four days, as potentially observed at SLOPE, a regional mode-1 M_2 phase speed of $c_1 \sim 3.0$ m s^{-1} (Zhao et al., 2016) suggests a baroclinic generation site up to 1000 km away. A likely candidate is the Mendocino Escarpment running east-west off of Northern California, one of the strongest generation sites for low-mode semidiurnal IT in the northeast Pacific (Althaus et al., 2003; Arbic et al., 2012; Zhao et al., 2017; Morozov, 2018). Strong tide-topography generated northward propagating mode-1 M_2 IT, along with the escarpment's location about 800 km due south of Barkley Canyon ($\sim$3.5 days), agree reasonably with the observed phase lag. Other potential semidiurnal IT generation sites are closer (e.g. the mouth of Juan de Fuca Strait $\sim$100 km, or the abyssal Juan de Fuca Ridge $\sim$400 km), or are somewhat obstructed by land (e.g. the Haida Gwaii Islands to the north), but could contribute.

Furthermore, for free incident semidiurnal IT, the criticality of the impacted topography can lead to focusing, breaking, or reflection, contributing to the elevated near-topography turbulent layers observed. Barkley Canyon is generally supercritical or near-critical to incident semidiurnal IT (Figure 4). Critical slope regions were determined from the gradient of bathymetric data obtained from the National Oceanic and Atmospheric Administration (NOAA) National Centre for Environmental Information, as 3 arc-second resolution mean sea level depth. At the SLOPE mooring, the local slope is $\beta \approx 0.060$, supercritical to the semidiurnal propagation angle $\alpha_{M2} \approx 0.026$ at that depth (Figure 5). This suggests reflection and focusing of incident semidiurnal IT, as observed. The SLOPE mooring sits adjacent to a large near-critical region below the shelf-break (Figure 4), which, along with the VICS itself, is a source of semidiurnal energy (Drakopoulos & Marsden, 1993). At other slope sites, there is evidence of elevated near-bottom energy-flux associated with both semidiurnal IT generation and incident reflection, with similar vertical scales within a few

hundred metres above bottom (Terker et al., 2014; Xie & Chen, 2021). For the AXIS mooring on the canyon floor, local criticality is $\beta \approx 0.019 < \alpha_{M2} \approx 0.036$ (Figure 5). As such, this portion of the canyon floor is subcritical to incident semidiurnal IT, scattering energy along-canyon. However, as the canyon walls are generally supercritical, and the surrounding floor is near-critical (Figure 4), the propagation (and generation) of semidiurnal IT at AXIS is likely complex. Xu and Noble (2009) found that deep in Monterey Canyon semidiurnal IT were not only scattered up-canyon along the subcritical floor, but also reflected down by the supercritical walls, highly focusing semidiurnal energy near the bottom. The potential for scattering, reflection, focusing, and generation of semidiurnal IT all near the AXIS mooring could lead to the observed highly 'channeled' deep-canyon semidiurnal response.

Together, the irregular nature of the semidiurnal spring-neap phase-lag and the potential for critical IT-topography interactions suggests that forcing is a mix of local barotropic and incident IT. As the barotropic tide passes over Barkley Canyon, near-critical slope and canyon topography generate and focus semidiurnal IT. Remote incident IT are also subject to these effects, and alter observed spring-neap phase based on their origin, likely Mendocino Escarpment to the south. Finally, as the weak annual seasonality in barotropic spring-neap forcing cannot explain observed large-scale inter-annual features, such as the subtle yet consistent spring increase in semidiurnal energy at SLOPE, there may be contributing effects due to seasonal changes in stratification (Drakopoulos & Marsden, 1993; Cummins & Oey, 1997).

5.3 Near-inertial forcing

NI IW generated by wind events are thought to be significant contributors to mixing in the deep ocean, of similar magnitude to the conversion of barotropic tide to baroclinic internal tide energy (Alford et al., 2012). As such effective contributors to deep ocean energy, it is interesting that associated NI energy can be so strongly attenuated with depth at SLOPE, while still eliciting a deep response at AXIS. The timing of these events is qualitatively linked, so the difference in topography likely modulates the response. Thomson et al. (1990) found that NI IW become increasingly attenuated as they approach slopes, absorbed by strong vertical shear in the background flow associated with topographically trapped oscillations. Yet observed NI IW energy is enhanced near the canyon floor, not attenuated. Alford et al. (2016) note that canyon walls confine the typically circular motion of NI waves, forcing them rectilinearly along-canyon.

It may be that canyon topography uniquely effects the modal structure of

ML generated NI waves, as deep canyon NI energy appears disconnected from the surface. Mode-1 ML amplitudes up to 0.6 m s^{-1} occur after notable wind events, and while low modes generally dominate, more deep NI activity is observed when the ML is thin and high modes are prevalent, similar to findings by Jarosz et al. (2007) in DeSoto Canyon. Alford et al. (2016) note that high mode waves propagate downward and equatorward, while low mode waves contribute more to lateral propagation of NI energy. However, this observation may simply be coincidental with more relevant processes, such as enhanced NI energy transfer during periods of thin ML depth. Ultimately, the downward propagation of NI IW is difficult to characterise, as there are so many factors to consider - site-specific topography, complex ML processes, seasonal thermocline thickness, β-plane effects, and near-surface mesoscale vorticity adjusting local f_0 could all contribute (Alford et al., 2016). Potential secondary forcing could be mean currents or lee waves across the mouth or rim of the canyon, where topographic attenuation of downward NI energy may be reduced due to the relative openness of those areas, possibly leading to nonlinearities that could drive deep along-canyon NI currents (Alford et al., 2016).

Regarding the delayed NI deep response to wind events, D'Asaro (1995) made a similar observation of an 8-10 day event, and theorised that divergence-forced NI pumping at the ML base causes oscillating pressure gradients in the pycnocline, accelerating NI currents at depth. The rate and mechanism of vertical energy transfer depends on the initial horizontal scale of the ML NI currents, with smaller horizontal scale currents propagating vertical energy faster (D'Asaro, 1995; Zervakis & Levine, 1995). For large-scale ML NI currents, vertical energy propagation is explained as the interference of low modes with higher modes that have frequencies closer to f, called 'inertial beating' (Gill, 1984; Zervakis & Levine, 1995). For small-scale ML NI currents, it is the timing of the horizontal departure of low modes that coincides with vertical energy propagation (Zervakis & Levine, 1995). There is a notable maximum associated with a timescale of the departure of modes 1 and 2 (up to 10-20 days), after which the deep response rapidly increases and NI energy is evenly distributed between the upper pycnocline and lower depths (Zervakis & Levine, 1995).

The inconsistent results between canyon sites suggest that NI forcing is highly complex, dependent on variable characteristics of wind events, ML processes, and site-specific topography, leading to intermittent seasonality below the pycnocline. Remote forcing is also possible, as free NI IW generated at the base of the surface mixed-layer must propagate equatorward due to the effects of turn-

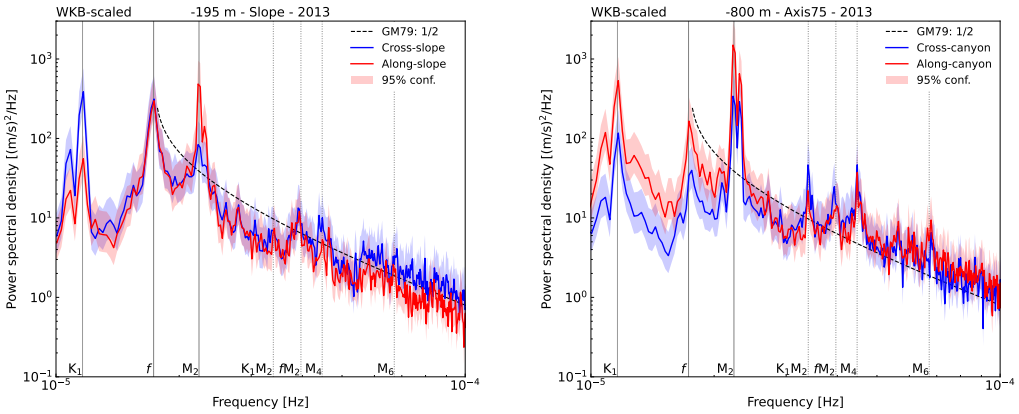

Figure 31. High frequency-resolution mid-depth PSD of WKB-scaled horizontal velocity data, for SLOPE (left) and AXIS (right), in 2013. Frequency scale is zoomed to the tidal range. There are no additional peaks or apparent blue-shift for the NI constituent, suggesting local or same-latitude forcing.

ing latitudes (Alford et al., 2016). There is often a blue-shift of the f spectral peak associated with remote NI forcing (Garratt, 1977; Voelker et al., 2020). High frequency-resolution spectra (Figure 31) do not resolve any blue-shift of NI peaks, though there is some higher-frequency broadening of the NI peak at AXIS. This suggests a combination of forcing due to local, same-latitude, or remote wind events, that may be uniquely modulated by the canyon. Further complicating analysis, strong qualitative and moderate quantitative correlations suggest that deep observations are most responsive to wind events in the late-summer and fall when the ML is thin, possibly coinciding with greater high-mode contributions or NI energy transfer. To summarise the efficacy of attempting to characterise vertical NI processes, Alford et al. (2016), when discussing the foundational Ocean Storms Experiment (D'Asaro, 1995), stated that "neither the decay of mixed-layer motions nor the rate of energy transfer into the deep ocean can adequately be predicted for the best-documented storm response on record". Needless to say, additional research is necessary.

5.4 Continuum-dissipation estimates

Topographic focusing of low-frequency IW and IT enhances energy, elevating the high-frequency continuum amplitude and driving mixing (Polzin, 2004). This is indicated by the heightened amplitudes and steep spectral slopes of the observed high-frequency continuum, as compared to open-ocean GM values (Figure 25). As IW energy cascades from low- (tidal and sub-inertial) to high-frequency processes, continuum energy variability should reflect this

transfer (Polzin, 2004). At both sites, high-frequency continuum energy variability correlations and power law fits indicate the semidiurnal constituent is the greatest contributor to dissipation. Secondary contributors are the subdiurnal band at SLOPE, and NI band at AXIS. There are likely lesser contributions from other constituents. For continental slopes, mean currents and semidiurnal IT have both been noted to contribute to increased near-bottom dissipation rates (Nash et al., 2007; Kunze et al., 2012), as observed here. Similarly, in submarine canyons, the semidiurnal constituent has been found to be the primary contributor to seasonal, near-bottom mixing (Kunze et al., 2002; Waterhouse et al., 2017). However, there is a lack of evidence for the observed deep-canyon NI IW energy, as discussed in Section 5.3. Also evident is the non-isotropic nature of the high-frequency continuum, in contrast to a theoretical GM open-ocean IW field, though this departure from theory is not surprising considering the strong topographic guiding of flow.

Winding canyons are hot spots for turbulence, as the reflection of IW at rough topography generates dissipation and scattering (Thorpe, 2001). Near topography in Monterey Canyon, Kunze et al. (2002) found spring-neap dependent average turbulent dissipation rates from 10^{-9} to 10^{-6} W kg^{-1} and diffusivity from 10^{-6} to 10^{-2} m^2 s^{-1}, respectively, consistent with other studies (Carter & Gregg, 2002) and similar to those observed here ($\varepsilon \sim 10^{-8}$ W kg^{-1} and $\kappa \sim 10^{-5}$ m^2 s^{-1}). Carter and Gregg (2002) used observed values from Monterey Canyon for stratified turbulent layer thickness ($\sim$ 135 m), ε (1.36×10^{-6} W kg^{-1}), and global approximations of shelf length occupied by canyons (15,500 km) and canyon length (20 km) to estimate global dissipation in canyons as roughly 56 GW, or 16% of global internal tide dissipation. Using this method and ε observations from the lower extent of the AXIS turbulent layer ($\varepsilon \sim 10^{-7}$ W kg^{-1}) results in an estimate of only 4 GW of global dissipation in canyons, or 1% of global internal tide dissipation. This disparity indicates that individual canyon topography strongly affects dissipation rates, and assumptions for global mixing budgets require further constraints. However, the observations by Kunze et al. (2002) and Carter and Gregg (2002) use multiple moorings to better estimate average dissipation in the Monterey Canyon stratified turbulent layer, as compared to the single mooring at AXIS, making this a tenuous comparison.

As it is difficult to quantify turbulence, it is hoped that a connection to semidiurnal (and secondary constituent) energy may be useful for models that may not have access to data that can resolve such high-frequency processes, in slope and canyon regions. The multivariate power law fits were found to be $\varepsilon \sim M_2^{0.83\pm0.17} + \mathrm{Sub}_{K1}^{0.59\pm0.13}$ and $\varepsilon \sim M_2^{1.47\pm0.48} + \mathrm{NI}^{0.24\pm0.06}$, for SLOPE and

AXIS, respectively. This builds on similar results by Klymak et al. (2006) at the Hawaiian Ridge, who found that near the ridge dissipation scaled with semidiurnal energy as $\varepsilon \sim M_2^{1.0\pm0.5}$. However, it is not enough to link dissipation to IW and IT driven high-frequency continuum energy, alone, as there are many spatially and temporally variable regional processes that may also contribute, such as large-scale ocean circulation, biogeochemical cycles, weather, and long-term climate (Kunze, 2017). Furthermore, turbulence may be forced intermittently by these phenomena (Klymak et al., 2006), making it difficult to attribute individual contributors over long periods. Use of the observed fits for modelling should be considered with these issues in mind, and improvements could be the subject of further research.

5.5 Near-N spectral shoulder energy

The near-N spectral shoulder is a well known, yet often unresolved feature in ADCP velocity spectra. As early as 1966, Sabinin described a prominent near-N peak that widened with depth, ascribed to IW-buoyancy ringing (Pinkel, 1975), yet beyond the next decade subsequent observations are brief (Kase & Clarke, 1978), and temporally sparse (D'Asaro et al., 2007; Pinkel, 2014; Alford et al., 2016). The long-term, high-frequency sampling in this study allows for a high Nyquist frequency and low noise floor that fully expose the shoulder, continuing the discussion. Observations indicate that shoulder energy is intermittently depth dependent at SLOPE, and more uniformly so at AXIS, similar to Pinkel's (1975) findings. There is subtle shoulder energy variability at both sites, being generally stronger in the fall, with correlations and power law fits suggesting that shoulder energy is tied to the high-frequency continuum, and therefore dissipation. This agrees with previous theories, arguing that the near-N shoulder is a result of an enhanced cascade of energy from low- to high-frequency turbulent processes due to resonant wave-wave interaction, where energy collects at and above the "resonant buoyancy frequency" (Leder, 2002) - approximately the depth-mean value of N below the buoyancy variable thermocline. In this study, $N_0 = 4.03 \times 10^{-4}$ Hz (averaged around -900 m and varying insubstantially when expanded to the lower thermocline), central to the observed shoulder, and similar to the ∼2 cph value of N_0 that defined the spectral shoulder (2 - 5 cph) of Kase and Clarke (1978), who modelled the near-N response with data from the GATE experiment.

However, seasonal forcing of the near-N spectral shoulder is inconsistent between studies. At Barkley Canyon, correlations and power law fits suggest that high-frequency continuum energy is strongly linked to spectral shoulder energy. As these power law fits overlap within uncertainty for both sites (averaging $P_{Sh} \sim \varepsilon^{0.34\pm0.08}$), it is possible that this relationship is independent of

site topography, likely due to the relatively small spatial scale of near-N motions. Furthermore, as high-frequency continuum energy is strongly suspected to cascade from the semidiurnal constituent (and partially from secondary contributors), the same forcing should apply to the spectral shoulder as the cascade continues. Leder (2002) suggested that solitons forming in the troughs of semidiurnal IT could contribute to near-N energy, but that it is unlikely, and evidence against this theory was provided by D'Asaro et al. (2007) who found no association between shoulder energy and observed solibores. Furthermore, there are no obvious solibores noted in the Barkley Canyon observations. Pinkel (2014) suggested that sub-mesoscale currents could contribute to near-N energy, and both Leder (2002) and Alford et al. (2016) attributed enhanced high-frequency shear to wind-forced NI IW. Forcing by these constituents agrees roughly with the possible secondary contributors to observed high-frequency continuum energy (sub-diurnal at SLOPE, and NI at AXIS), but is conspicuously lacking semidiurnal influence. It is possible that the near-N spectral shoulder does receive energy from the high-frequency continuum, but that turbulent processes are so variable, regionally, that forcing is unique to each study site. Properly quantifying the nature of this enhanced cascade of energy is important for better understanding the effects of turbulence and mixing, and is left for further study.

6 Summary and conclusions

It was found that there is significant influence from topography on the local IW field at both sites. Continental slope and canyon topography guides flow, with inter-annually consistent, periodic (about a week) up-canyon mean currents (-700 to -900 m) above a near-bottom down-canyon layer. There is frequency-dependent focusing of IW energy, generally up to a factor of 10, 130 m above bottom at SLOPE, and up to a factor of 100, 230 m above bottom at AXIS. The near-topography elevated energy has unique seasonality for individual frequency constituents, and varies little inter-annually. Sub-diurnal and diurnal flows are presumably sub-inertially trapped along topography, and the diurnal band appears to be forced locally (barotropically). The NI band is attenuated near the slope, yet elevated near the canyon bottom, with intermittent forcing that appears linked to regional wind events, high-mode propagation, and the seasonal ML depth. Free semidiurnal IT are focused and reflected near critical topography, and appear to experience both local and remote (baroclinic) forcing. The high-frequency IW continuum is elevated compared to the open-ocean GM spectrum (up to 7× GM), with enhanced dissipation (reaching 10^{-7} W kg^{-1}) and diffusivity (reaching 10^{-3} m^2 s^{-1}) near topography. Dissipation−band-power variability correlations suggest a cascade of energy from the semidiurnal constituent, yielding inter-annual power law fits of $\varepsilon \sim M_2^{0.42\pm0.29}$ at SLOPE, and $\varepsilon \sim M_2^{0.64\pm0.30}$ at AXIS. Improved fits accounting for secondary constituents yield power law relationships of $\varepsilon \sim M_2^{0.83\pm0.17}$+ $\mathrm{Sub}_{K1}^{0.59\pm0.13}$ at SLOPE, and $\varepsilon \sim M_2^{1.47\pm0.48}$+ $\mathrm{NI}^{0.24\pm0.06}$ at AXIS. There is evidence of a near-N spectral shoulder which may collect energy from high-frequency continuum turbulence, possibly an additional step in the cascade of energy from low- to high-frequency dissipative processes. The shoulder-dissipation energy variability correlations yield an average, site-independent power law fit of $P_{Sh} \sim \varepsilon^{0.34\pm0.08}$.

Unfortunately, the WKB-stretch scaling applied throughout much of the analysis is based on deep CTD casts that were made nearby (20 km south of Barkley Canyon), but away from topography. The stratification profile captures the surface ML and pycnocline, but does not account for adjustment near the slope or in the canyon (Figure 9). Hotchkiss and Wunsch (1982) noted increased stratification near areas of high 'topographic relief', such as the shelf-break and slopes. These highly stratified turbulent layers may more strongly experience the effects of reflection, scattering, and IT and lee-wave generation, as well as amplification of IW and IT. To properly account for the effects of depth-dependent stratification variability, further research would benefit from site specific climatology data.

Results could be further improved through increased sampling consistency between instruments (there were maintenance periods and instrument redeployments during analysis years), additional instrument sites (along the length of the canyon floor and rim), and additional overlapping comparison years between sites. Broader temporal coverage could provide insight into long-term seasonality, while additional spatial coverage would allow for observations of IW propagation. For NI wind forcing, reanalysis wind data may have provided better (fewer gaps) temporal coverage for comparison.

Further research is required to: identify forcing for the sub-diurnal range's intermittent seasonality and the periodicity of up-canyon mean currents at AXIS; accurately identify sites of origin for incident baroclinic shelf waves and IT affecting the diurnal and semidiurnal responses; better quantify the downward propagation of NI IW energy from the ML to the interior; profile the attenuation of NI energy from the surface to deep canyon; and, improve power law fits of dissipation and near-N spectral shoulder energy to better model the cascade of energy from low- to high-frequency turbulent mixing.

Barkley Canyon is a dynamic continental slope and submarine canyon region with physical processes that are heavily influenced by topography. Continental slopes and canyons are known as hot-spots for IT generation and IW-driven turbulence, contributing significantly to regional transport of energy, shelf productivity, and even large-scale ocean circulation and climate effects. As regional currents, tides, and wind all contribute to an energetic local IW field, the Barkley Canyon portion of ONC's NEPTUNE cabled observatory is an important data network for understanding the effects of topography-IW interactions on the VICS. Furthermore, results here may be valuable for characterising mixing processes at other slope and canyon sites, and for better estimating the global IW and IT energy budget. It is hoped that this study has provided valuable insight leading to further research and collaboration, and improved knowledge of the importance of shelf-incising canyon regions as fundamental to both regional and large-scale physical ocean processes.

7 References

Alford, M. H. (2001). Internal swell generation: The spatial distribution of energy flux from the wind to mixed layer near-inrtial motions. Journal of Physical Oceanography, 31(8 PART 2), 2359–2368.

Alford, M. H., MacKinnon, J. A., Zhao, Z., Pinkel, R., Klymak, J., & Peacock, T. (2007). Internal waves across the Pacific. Geophysical Research Letters, 34(24), 24601.

Alford, M. H. (2003). Improved global maps 54-year history of wind-work on ocean inertial motions. Geophysical Research Letters, 30(8), 1424.

Alford, M. H. (2020). Revisiting near-inertial wind work: Slab models, relative stress, and mixed layer deepening. Journal of Physical Oceanography, 50(11), 3141–3156.

Alford, M. H., Cronin, M. F., & Klymak, J. M. (2012). Annual cycle and depth penetration of wind-generated near-inertial internal waves at ocean station papa in the northeast pacific. Journal of Physical Oceanography, 42(6), 889–909.

Alford, M. H., Mackinnon, J. A., Simmons, H. L., & Nash, J. D. (2016). Near-Inertial Internal Gravity Waves in the Ocean. Annual Review of Marine Science, 8, 95–123.

Alford, M. h., Shcherbina, A. Y., & Gregg, M. C. (2013). Observations of Near-Inertial Internal Gravity Waves Radiating from a Frontal Jet. Journal of Physical Oceanography, 43(6), 1209–1224.

Alford, M. H., & Zhao, Z. (2007). Global patterns of low-mode internal-wave propagation. Part I: Energy and energy flux. Journal of Physical Oceanography, 37(7), 1829–1848.

Allen, S. E., Vindeirinho, C., Thomson, R. E., Foreman, M. G. G., & Mackas, D. L. (2001). Physical and biological processes over a submarine canyon during an upwelling event. Canadian Journal of Fisheries and Aquatic Sciences, 58(4), 671–684.

Althaus, A. M., Kunze, E., & Sanford, T. B. (2003). Internal tide radiation from Mendocino escarpment. Journal of Physical Oceanography, 33(7), 1510–1527.

Anstey, K. (2022). *Internal waves at Barkley Canyon.* GitHub. https://github.com/kurtisanstey/internal_waves_barkley_canyon

Arbic, B. K., Richman, J. G., Shriver, J. F., Timko, P. G., Joseph Metzger, E., & Wallcraft, A. J. (2012). Global modeling of internal tides within an eddying ocean general circulation model. Oceanography, 25(2), 20–29.

Brink, K. H. (1991). Coastal-trapped waves and wind-driven currents over the continental shelf. Annual Review of Fluid Mechanics, 23(1), 389–412.

Burrier, D. A. (2019). The Internal Wave Dynamics of Barkley Submarine Canyon. San Jose State University.

Cabrera, F., Ogata, B., Sastri, A. R., Heesemann, M., Mihály, S., Galbraith, M., & Morley, M. G. (2018). High-frequency observations from a deep-sea cabled observatory reveal seasonal overwintering of Neocalanus spp. in Barkley Canyon, NE Pacific: Insights into particulate organic carbon flux. Progress in Oceanography, 169, 120–137.

Callies, J. (2019). *GM81.* GitHub. https://github.com/joernc/GM81

Canadian Hydrographic Service (CHS). (2020). *Tofino (8615) water levels.* Station Inventory Data. https://www.isdm-gdsi.gc.ca/isdm-gdsi/twl-mne/inventory-inventaire/sd-ds-eng.asp?no=8615&user=isdm-gdsi&region=PAC

Carter, G. S., & Gregg, M. C. (2002). Intense, variable mixing near the head of Monterey Submarine Canyon. In Journal of Physical Oceanography (Vol. 32).

Chauvet, P., Metaxas, A., Hay, A. E., & Matabos, M. (2018). Annual and seasonal dynamics of deep-sea megafaunal epibenthic communities in Barkley Canyon (British Columbia, Canada): A response to climatology, surface productivity and benthic boundary layer variation. Progress in Oceanography, 169, 89–105.

Crawford, W. R. (1984). Energy flux and generation of diurnal shelf waves along Vancouver Island. J. Phys. Oceanogr., 14(10, Oct. 1984), 1600–1607.

Crawford, W. R., & Thomson, R. E. (1984). Diurnal-Period Continental Shelf Waves along Vancouver Island: A Comparison of Observations with Theoretical Models. Journal of Physical Oceanography, 14(10), 1629–1646.

Cummins, P. F., Masson, D., & Foreman, M. G. G. (2000). Stratification and mean flow effects on diurnal tidal currents off Vancouver Island. Journal of Physical Oceanography, 30(1), 15–30.

Cummins, P. F., & Oey, L. Y. (1997). Simulation of barotropic and baroclinic

tides off northern British Columbia. Journal of Physical Oceanography, 27(5), 762–781.

D'Asaro, E. A. (1985). The energy flux from the wind to near-inertial motions in the surface mixed layer. J. Phys. Oceanogr., 15(8, Aug. 1985), 1043–1059.

D'Asaro, E. A. (1995). Upper-ocean inertial currents forced by a strong storm. Part III: interaction of inertial currents and mesoscale eddies. Journal of Physical Oceanography, 25(11 Part II), 2953–2958.

D'Asaro, E. A., Lien, R. C., & Henyey, F. (2007). High-frequency internal waves on the Oregon continental shelf. Journal of Physical Oceanography, 37(7), 1956–1967.

Doya, C., Aguzzi, J., Pardo, M., Matabos, M., Company, J. B., Costa, C., ... Canals, M. (2014). Diel behavioral rhythms in sablefish (Anoplopoma fimbria) and other benthic species, as recorded by the Deep-sea cabled observatories in Barkley canyon (NEPTUNE-Canada). Journal of Marine Systems, 130, 69–78.

Drakopoulos, P. G., & Marsden, R. F. (1993). The internal tide off the west coast of Vancouver Island. Journal of Physical Oceanography, 23(4), 758–775.

Fisheries and Oceans Canada (DFO). (2020). *LB14 CTD data.* Water Properties. https://www.waterproperties.ca/data/

Fisheries and Oceans Canada (DFO). (2021). *46206 buoy data.* Marine Environmental Data. https://www.meds-sdmm.dfo-mpo.gc.ca/isdm-gdsi/waves-vagues/data-donnees/data-donnees-eng.asp?medsid=C46206

Flather, R. A. (1988). A numerical model investigation of tides and diurnal-period continental shelf waves along Vancouver Island. J. Phys. Oceanog r., 18(1, Jan. 1988), 115–139.

Garratt, J. R. (1977). Review of Drag Coefficients over Oceans and Continents. Monthly Weather Review, 105(7), 915–929.

Garrett, C., & Kunze, E. (2007). Internal tide generation in the deep ocean. Annual Review of Fluid Mechanics, 39, 57–87.

Garrett, C. (2005). 2004 Program of Study: Tides Course Lectures Fellows Project Reports.

Gemmrich, J., & Klymak, J. M. (2015). Dissipation of internal wave energy

generated on a critical slope. Journal of Physical Oceanography, 45(9), 2221–2238.

Gill, A. E. (1984). On the Behavior of Internal Waves in the Wakes of Storms. Journal of Physical Oceanography, 14(7), 1129–1151.

Gonella, J. (1972). A rotary-component method for analysing meteorological and oceanographic vector time series. In Deep-Sea Research and Oceanographic Abstracts (Vol. 19).

Gregg, M. C. (1989). Scaling turbulent dissipation in the thermocline. Journal of Geophysical Research, 94(C7), 9686.

Hotchkiss, F. S., & Wunsch, C. (1982). Internal waves in Hudson Canyon with possible geological implications. Deep Sea Research Part A, Oceanographic Research Papers, 29(4), 415–442.

Jarosz, E., Hallock, Z. R., & Teague, W. J. (2007). Near-inertial currents in the DeSoto Canyon region. Continental Shelf Research, 27(19), 2407–2426.

Juniper, S. K., Matabos, M., Mihály, S., Ajayamohan, R. S., Gervais, F., & Bui, A. O. V. (2013). A year in Barkley Canyon: A time-series observatory study of mid-slope benthos and habitat dynamics using the NEPTUNE Canada network. Deep-Sea Research Part II: Topical Studies in Oceanography, 92, 114–123.

Käse, R. H., & Allyn Clarke, R. (1978). High frequency internal waves in the upper thermocline during GATE. Deep-Sea Research, 25(9), 815–825.

Klymak, J. M., Alford, M. H., Pinkel, R., Lien, R. C., Yang, Y. J., & Tang, T. Y. (2011). The breaking and scattering of the internal tide on a continental slope. Journal of Physical Oceanography, 41(5), 926–945.

Klymak, J. M., Moum, J. N., Nash, J. D., Kunze, E., Girton, J. B., Carter, G. S., ... Gregg, M. C. (2006). An estimate of tidal energy lost to turbulence at the Hawaiian Ridge. Journal of Physical Oceanography, 36(6), 1148–1164.

Kundu, P. K., & Cohen, I. (2008). Fluid mechanics. (4th ed.). Academic Press.

Kunze, E. (1985). Near-Inertial Wave Propagation In Geostrophic Shear. Journal of Physical Oceanography, 15(5), 544–565.

Kunze, E. (2017). Internal-wave-driven mixing: Global geography and budgets. Journal of Physical Oceanography, 47(6), 1325–1345.

Kunze, E., Mackay, C., Mcphee-Shaw, E. E., Morrice, K., Girton, J. B., & Terker, S. R. (2012). Turbulent mixing and exchange with interior waters on sloping boundaries. Journal of Physical Oceanography, 42(6), 910–927.

Kunze, E., Rosenfeld, L. K., Carter, G. S., & Gregg, M. C. (2002). Internal waves in Monterey Submarine Canyon. Journal of Physical Oceanography, 32(6), 1890–1913.

Le Souëf, K. E., & Allen, S. E. (2014). Physical modeling of tidal resonance in a submarine canyon. Journal of Geophysical Research: Oceans, 119(2), 1324–1343. https://doi.org/10.1002/2013JC009612

Lamb, K. G. (2014). Internal wave breaking and dissipation mechanisms on the continental slope/shelf. Annual Review of Fluid Mechanics, 46, 231–254.

Lavelle, J. W., & Cannon, G. A. (2001). On subinertial oscillations trapped by the Juan de Fuca Ridge, northeast Pacific. In Journal of Geophysical Research: Oceans (Vol. 106).

Leder, N. (2002). Wind-induced internal wave dynamics near the Adriatic shelf break. In Continental Shelf Research (Vol. 22).

Levine, M. D. (2002). A modification of the Garrett-Munk internal wave spectrum. Journal of Physical Oceanography, 32(11), 3166–3181.

Li, M., Myers, P. G., & Freeland, H. (2005). An examination of historical mixed layer depths along Line P in the Gulf of Alaska. Geophysical Research Letters, 32(5), 1–4.

Martini, K. I., Alford, M. H., Kunze, E., Kelly, S. M., & Nash, J. D. (2011). Observations of internal tides on the oregon continental slope. Journal of Physical Oceanography, 41(9), 1772–1794.

Martini, K. I., Alford, M. H., Kunze, E., Kelly, S. M., & Nash, J. D. (2013). Internal bores and breaking internal tides on the Oregon continental slope. Journal of Physical Oceanography, 43(1), 120–139.

Mihaly, S. F., Thomson, R. E., & Rabinovich, A. B. (1998). Evidence for nonlinear interaction between internal waves of inertial and semidiurnal frequency. Geophysical Research Letters, 25(8), 1205–1208.

Morozov, E. G. (2018). Semidiurnal Internal Wave Global Field; Global Estimates of Internal Tide Energy. In Oceanic Internal Tides: Observations, Analysis and Modeling (pp. 263-291).

Munk, W., & Garrett, C. (1979). Internal Waves and Small-Scale Processes. In C. Wunsch (Ed.), Evolution of Physical Oceanography.

Munk, W., & Wunsch, C. (1998). Abyssal recipes II: Energetics of tidal and wind mixing. Deep-Sea Research Part I: Oceanographic Research Papers, 45(12), 1977–2010.

Nash, J. D., Kunze, E., Toole, J. M., & Schmitt, R. W. (2004). Internal tide reflection and turbulent mixing on the continental slope. In Journal of Physical Oceanography (Vol. 34).

National Oceanic and Atmospheric Association (NOAA). (2021). *Bathymetric data viewer.* National Centers for Environmental Information. https://www.ncei.noaa.gov/maps/bathymetry/

Nortek. (2020). *Signature55 technical specifications.* Current Profilers. https://www.nortekgroup.com/products/signature55

Ocean Networks Canada (ONC). (2019). *Barkley Canyon Axis and Slope ADCP data.* Oceans 2.0. https://data.oceannetworks.ca/DataSearch

Osborn, T. R. (1980). Estimates of the Local Rate of Vertical Diffusion from Dissipation Measurements. J. Phys. Oceanogr., 10(Jan 1980), 83–89.

Petruncio, E. T., Rosenfeld, L. K., & Paduan, J. D. (1998). Observations of the internal tide in Monterey Canyon. Journal of Physical Oceanography, 28(10), 1873–1903.

Pinkel, R. (1975). Upper ocean internal wave observations from Flip. Journal of Geophysical Research, 80(27), 3892–3910.

Pinkel, R. (2014). Vortical and internal wave shear and strain. Journal of Physical Oceanography, 44(8), 2070–2092.

Polzin, K. L., & Lvov, Y. V. (2011). Toward regional characterizations of the oceanic internal wavefield. Reviews of Geophysics, 49(4), 4003.

Polzin, K. L., Toole, J. M., Ledwell, J. R., & Schmitt, R. W. (1997). Spatial variability of turbulent mixing in the abyssal ocean. Science, 276(5309), 93–96.

Polzin, K. (2004). A heuristic description of internal wave dynamics. Journal of Physical Oceanography, 34(1), 214–230.

Rainville, L., & Pinkel, R. (2006). Propagation of low-mode internal waves through the ocean. In Journal of Physical Oceanography (Vol. 36). https://doi.org/10.1175/JPO2889.1

Robertson, R., Dong, J., & Hartlipp, P. (2017). Diurnal Critical Latitude and the Latitude Dependence of Internal Tides, Internal Waves, and Mixing Based on Barcoo Seamount. Journal of Geophysical Research: Oceans, 122(10), 7838–7866.

Rudnick, D. L., Gopalakrishnan, G., & Cornuelle, B. D. (2015). Cyclonic eddies in the Gulf of Mexico: Observations by underwater gliders and simulations by numerical model. Journal of Physical Oceanography, 45(1), 313–326.

Sun, H., & Kunze, E. (1999). Internal wave-wave interactions. Part I: The role of internal wave vertical divergence. Journal of Physical Oceanography, 29(11), 2886–2904.

Teledyne Marine (RDI). (2020). *Workhorse Long Ranger ADCP.* RD Instruments. http://www.teledynemarine.com/workhorse-long-ranger-adcp

Terker, S. R., Girton, J. B., Kunze, E., Klymak, J. M., & Pinkel, R. (2014). Observations of the internal tide on the California continental margin near Monterey Bay. Continental Shelf Research, 82, 60–71.

Thomson, R. E., & Crawford, W. R. (1982). The Generation of Diurnal Period Shelf Waves by Tidal Currents in: Journal of Physical Oceanography Volume 12 Issue 7 (1982). Journal of Physical Oceanography, 12(7).

Thomson, R. E., & Emery, W. J. (2014). Data Analysis Methods in Physical Oceanography: Third Edition. In Data Analysis Methods in Physical Oceanography: Third Edition (Third).

Thomson, R. E., & Fine, I. V. (2003). Estimating mixed layer depth from oceanic profile data. Journal of Atmospheric and Oceanic Technology, 20(2), 319–329.

Thomson, R. E., & Krassovski, M. V. (2015). Remote alongshore winds drive variability of the California Undercurrent off the British Columbia-Washington coast. Journal of Geophysical Research: Oceans, 120(12), 8151–8176.

Thomson, R. E., Roth, S. E., & Dymond, J. (1990). Near-inertial motions over a mid-ocean ridge: Effects of topography and hydrothermal plumes. Journal of Geophysical Research, 95(C5), 7261.

Thorpe, S. A. (2001). On the Reflection of Internal Wave Groups from Sloping Topography. Journal of Physical Oceanography, 31(10), 3121–3126.

Voelker, G. S., Olbers, D., Walter, M., Mertens, C., & Myers, P. G. (2020).

Estimates of wind power and radiative near-inertial internal wave flux: The hybrid slab model and its application to the North Atlantic. Ocean Dynamics, 70(11), 1357–1376.

Waterhouse, A. F., Mackinnon, J. A., Musgravea, R. C., Kelly, S. M., Pickering, A., & Nash, J. (2017). Internal tide convergence and mixing in a submarine canyon. Journal of Physical Oceanography, 47(2), 303–322.

Xie, X., & Chen, D. (2021). Near-surface reflection and nonlinear effects of low-mode internal tides on a continental slope. Journal of Physical Oceanography, 51(4), 1037–1051.

Xu, J. P., & Noble, M. A. (2009). Currents in monterey submarine canyon. Journal of Geophysical Research: Oceans, 114(3), 3004.

Zervakis, V., & Levine, M. D. (1995). Near-inertial energy propagation from the mixed layer: theoretical considerations. Journal of Physical Oceanography, 25(11 Part II), 2872–2889.

Zhai, X., Greatbatch, R. J., & Zhao, J. (2005). Enhanced vertical propagation of storm-induced near-inertial energy in an eddying ocean channel model. Geophysical Research Letters, 32(18), 1–4.

Zhao, Z., Alford, M. H., Girton, J. B., Rainville, L., & Simmons, H. L. (2016). Global observations of open-ocean mode-1 M2 internal tides. Journal of Physical Oceanography, 46(6), 1657–1684.

Zhao, Z. (2017). Propagation of the Semidiurnal Internal Tide: Phase Velocity Versus Group Velocity. Geophysical Research Letters, 44(23), 11942-11950.

Zheng, J., Tian, J., & Liang, H. (2017). Observation of near-inertial internal waves on the continental slope in the northwestern South China Sea. Journal of Ocean University of China, 16(2), 184–190.

A Appendix: Supplemental wind comparisons

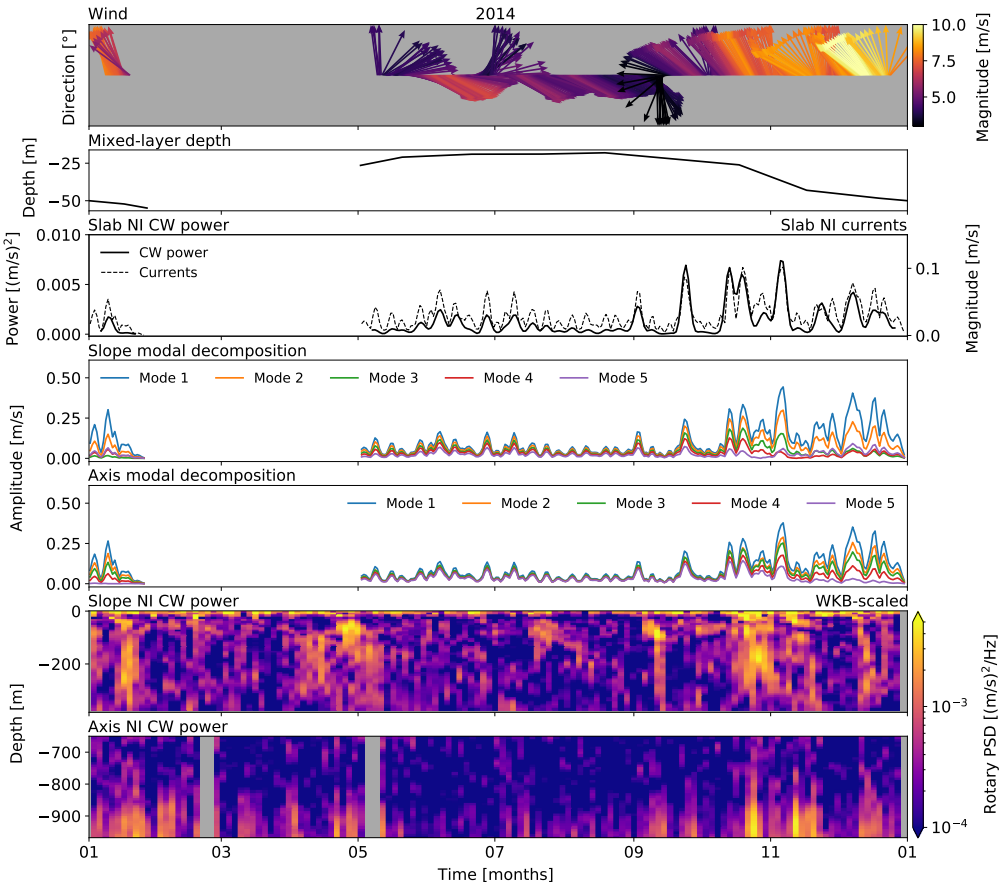

Figure 32. NI forcing analysis for 2014. From top to bottom: wind direction and amplitude; monthly-averaged ML depth for Line P station 3 as determined by Li et al. (2005); slab model NI CW power and NI currents; seasonal mode amplitudes for SLOPE and AXIS; and, band-integrated NI CW power at SLOPE and AXIS. There appears to be a complex relationship between the wind, ML, slab currents, and mode amplitudes in driving the NI observations, with the most obvious effects in the fall.

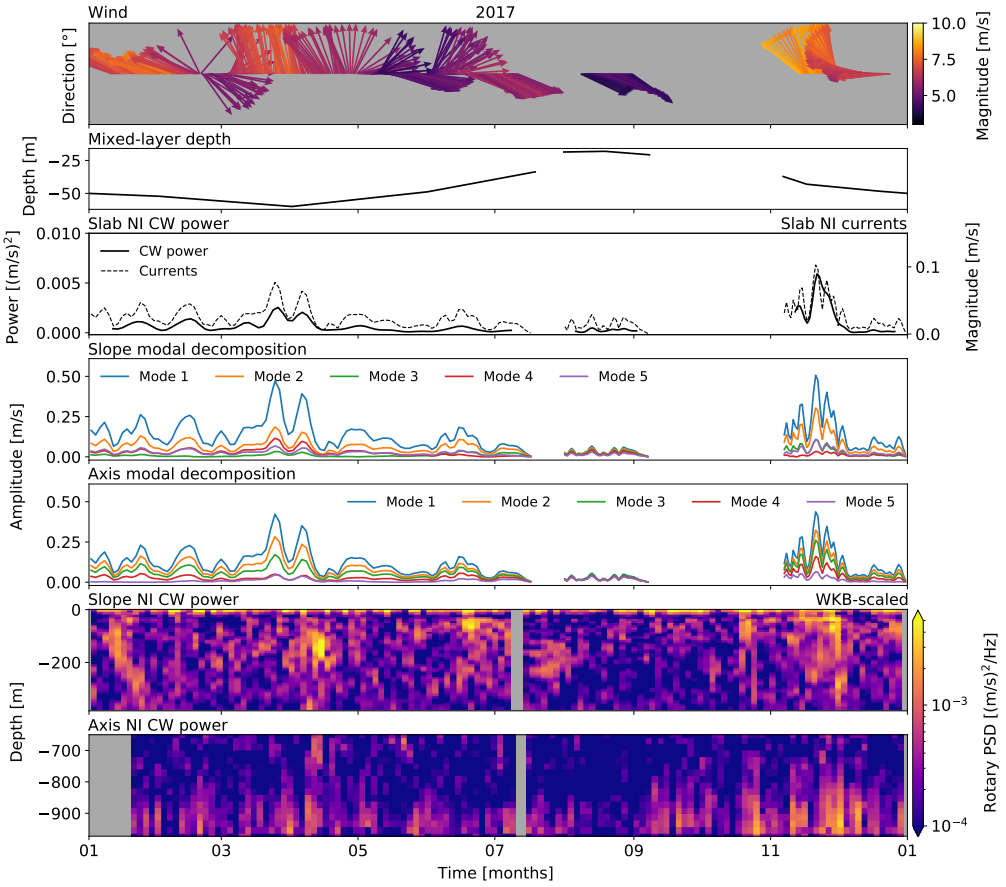

Figure 33. NI forcing analysis for 2017. From top to bottom: wind direction and amplitude; monthly-averaged ML depth for Line P station 3 as determined by Li et al. (2005); slab model NI CW power and NI currents; seasonal mode amplitudes for SLOPE and AXIS; and, band-integrated NI CW power at SLOPE and AXIS. There appears to be a complex relationship between the wind, ML, slab currents, and mode amplitudes in driving the NI observations, with the most obvious effects in the fall.

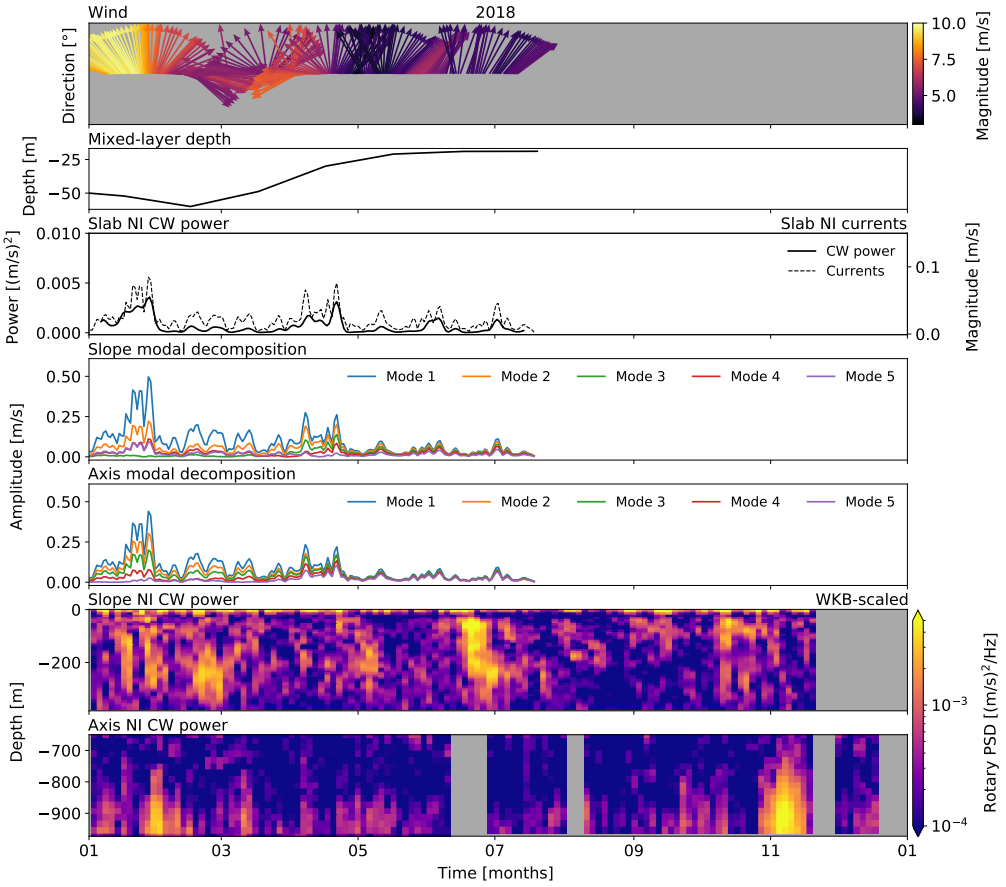

Figure 34. NI forcing analysis for 2018. From top to bottom: wind direction and amplitude; monthly-averaged ML depth for Line P station 3 as determined by Li et al. (2005); slab model NI CW power and NI currents; seasonal mode amplitudes for SLOPE and AXIS; and, band-integrated NI CW power at SLOPE and AXIS. There appears to be a complex relationship between the wind, ML, slab currents, and mode amplitudes in driving the NI observations, with the most obvious effects in the fall.